

Initial Design Investigation for 1310 nm VECSEL and Compensating Spatial Walk-off using  
Phase Shifted Astigmatic Mode Converter

Jacob Boyer

---

Copyright © Charles Johnson 2022

A Thesis Submitted to the Faculty of the

COLLEGE OF OPTICAL SCIENCES

In Partial Fulfillment of the Requirements

For the Degree of

MASTER OF SCIENCE

In the Graduate College

THE UNIVERSITY OF ARIZONA

2022

THE UNIVERSITY OF ARIZONA  
GRADUATE COLLEGE

As members of the Master's Committee, we certify that we have read the thesis prepared by **Jacob Nathaniel Boyer**, titled *Initial Design Investigation for 1310 nm VECSEL and Compensating Spatial Walkoff using Phase Shifted Astigmatic Mode Converter* and recommend that it be accepted as fulfilling the thesis requirement for the Master's Degree.

Mahmoud Fallahi Date: 8/4/2022  
Professor Mahmoud Fallahi

Stanley Pau Date: 8/4/2022  
Professor Stanley K. H. Pau

Chris Hessenius Date: 8/4/2022  
Professor Chris A. Hessenius

Final approval and acceptance of this thesis is contingent upon the candidate's submission of the final copies of the thesis to the Graduate College.

I hereby certify that I have read this thesis prepared under my direction and recommend that it be accepted as fulfilling the Master's requirement.

Mahmoud Fallahi Date: 8/4/2022  
Professor Mahmoud Fallahi  
Master's Thesis Committee Chair  
Wyant College of Optical Sciences

ARIZONA

# Acknowledgement

First and foremost, I would like to thank my wife, Michele. Without her support and understanding, this master's would not have been possible. She has been the structure that I can count on when balancing work, school, and life, and her contributions to this master's and all aspects of my life will never be forgotten. Secondly, I would like to thank Professor Mahmoud, Ph.D. Student Nathan Gottesman, Professor Chris Hassenius, Ph.D. Jason Meyer, and my committee members for their assistance and guidance throughout this masters. Professor Mahmoud and Nathan have worked with me for over a year to ensure that this master's was successful and their effort is appreciated. Chris Hassenius and Jason have been mentors that I can count on since my bachelor's degree. They have contributed time, energy, and patience to help me be successful in my career and academics. Thirdly, I want to thank my family. They have provided me with the support that I will never be able to repay, and my success in every aspect can be followed back to the support and lessons they have taught me throughout my life. Next, I would like to thank my friends for understanding the time requirement that this master's has taken and supporting me throughout this 4-year endeavor. Lastly, I would like to thank II-VI for giving the grant that allowed for me to able to research this thesis and to complete my master's degree.

# Table of Contents

<b>ACKNOWLEDGEMENT</b> .....	<b>3</b>
<b>TABLE OF FIGURES</b> .....	<b>5</b>
<b>ABSTRACT</b> .....	<b>7</b>
<b>TABLE OF ACRONYMS</b> .....	<b>8</b>
<b>CHAPTER 1: INTRODUCTION/ BACKGROUND</b> .....	<b>9</b>
1.1 INTRODUCTION/APPLICATION .....	9
1.1.1 Importance of 1310 nm wavelength.....	9
1.1.2 Orbital Angular Momentum Applications.....	10
1.2 CRITICAL VECSEL ATTRIBUTES .....	12
1.2.1 Basics of VECSEL.....	12
1.2.2 VECSEL Power Capabilities.....	14
1.2.3 Higher Transverse Mode Beams/Laguerre Gaussian Beams.....	15
1.3 CONCLUSION.....	16
<b>CHAPTER 2: INITIAL LITERATURE REVIEW OF DESIGN OF 1310 NM VECSEL</b> .....	<b>17</b>
2.1 INTRODUCTION .....	17
2.2 THERMAL MANAGEMENT .....	21
2.3 DBR ( DISTRIBUTED BRAGG REFLECTOR).....	25
2.4 GAIN MEDIUM MULTI QUANTUM WELL MATERIAL EVALUATION .....	26
2.5 CONCLUSION.....	31
<b>CHAPTER 3: ABCD MATRIX SIMULATION OF V CAVITY PROFILE</b> .....	<b>32</b>
3.1 INTRODUCTION .....	32
3.2 ABCD MATRIX.....	35
3.2.1 Intro.....	35
3.2.2 ABCD Sample Matrices.....	38
3.3 ABCD BEAM PROFILE V- CAVITY VECSEL SIMULATION .....	40
<b>CHAPTER 4: COMPENSATING SPATIAL WALKOFF USING PHASE SHIFTED ASTIGMATIC MODE CONVERTER</b> .....	<b>43</b>
4.1 INTRODUCTION/ BACKGROUND.....	43
4.2 ASTIGMATIC MODE CONVERTER THEORY AND CODE SIMULATION .....	46
4.3 RESULTS AND ANALYSIS .....	48
<b>CHAPTER 5: CONCLUSIONS</b> .....	<b>52</b>
<b>REFERENCE</b> .....	<b>54</b>

# Table of Figures

Figure 1: Optical Loss vs Wavelength 1980's to Modern times[2].....	9
Figure 2: Helical wave fronts with associated Poynting Vector to produce orbital angular momentum [4] .....	10
Figure 3: Common multiplexing optical properties [5] .....	11
Figure 4: Crosstalk analysis of OAM with different multiplexing properties[5] .....	12
Figure 5: Two standard VECSEL Set ups, V-Cavity (LEFT) and Standard Cavity (Right) [6] .....	13
Figure 6: Multi-Quantum Well Active Region Semiconductor Structure[6].....	13
Figure 7: The Tuning Spectra of a set of VECSELs [8] .....	15
Figure 8: Output Power[W] vs net pump power[W] of a VECSEL operating at different Hermite-Gaussian and Laguerre Gaussian Transverse modes [8] .....	15
Figure 9: Different beam profiles of LG modes[12] .....	16
Figure 10: Experimental Beam Profile results of VECSEL's of LG Beams [7].....	16
Figure 11: Principle of operation of a semiconductor laser [13].....	18
Figure 12: Schematic illustrations of spontaneous emission(a), stimulated emission (b) and absorption(c) [13] .....	18
Figure 13: Diagram of double heterostructure laser [13].....	19
Figure 14: A diagram of a single quantum well heterostructure depicting the energy band versus position [13] .....	20
Figure 15: Diagram of MQW [13] .....	20
Figure 16: Diagram of VCSEL Structure [13] .....	20
Figure 17: Diagrams of fused gain mirror stack (a), intra-cavity diamond (b), and a flip-chip(c) thermal management methods[9].....	21
Figure 18: Results from a study investigating the different thermal management methods and capabilities [37] .....	22
Figure 19: Shows the average temperature rise in gain section versus pump power, with the first graph being 0.98 $\mu\text{m}$ disk laser and the second graph showing a 2.35 $\mu\text{m}$ disk laser [37] .....	22
Figure 20: Ratio of temperature in the heat spreader and thinned devices for different wavelengths with different semiconductor materials systems[37].....	23
Figure 21: Flip-Chip(thin device with diamond sub mount) vs Intracavity average temperature change in gain section [27].....	23
Figure 22: Table of Distributed Bragg reflector materials and properties [27].....	26
Figure 23: Emission Wavelengths of selected III -V and IV-VI compounds at 300k [17].....	27
Figure 24: Composition diagram of $\text{In}_{1-x}\text{Ga}_x\text{As}_y\text{P}_{1-y}$ [17].....	28
Figure 25: Energy bandgap versus lattice constant[18].....	29
Figure 26: Bandgap composition diagram for $\text{In}_{1-x}\text{Ga}_x\text{As}_y\text{P}_{1-y}$ lattice matched to InP[17] .....	29
Figure 27: Lattice constant and bandgap energy of $\text{Al}_x\text{Ga}_{1-x}\text{In}_y\text{As}_{1-y}$ quaternary system, left bottom corner is the indirect bandgap zone[19].....	30
Figure 28: Different laser resonators, first with flat parallel mirrors, second flat mirrors with non-parallel mirrors and thirdly resonators with curved mirrors[24] .....	33
Figure 29: Examples of stable resonators[24].....	33
Figure 30: Diagram of V-Cavity VECSEL[8] .....	34
Figure 31: Diagram of V-Cavity VECSEL[6] .....	34

Figure 32:Diagram of T-Cavity VECSEL with additional optical devices incorporated[7].....	35
Figure 33: Model of ray matrix formula [24].....	35
Figure 34: Model of the beam diagram and critical beam parameters[24] .....	38
Figure 35: Ray Matrices for some common cases [13] .....	39
Figure 36: Graphic User Interface of the ABCD Matrix Live Program .....	40
Figure 37: Diagram of spatial walk-off effect [32] .....	43
Figure 38: Experimental images of SHG beams including <i>HG01, HG02, HG11 and HG22</i> [33].....	44
Figure 39: Examples of the decomposition of HG and LG modes [34]. .....	44
Figure 40: Beam profile (a), a lens placed at the beam waist transverse radii (b), and two lenses placed at each of the beam waists transverse radii (c) .....	46
Figure 41: Beam Intensity Profile of HG and LG fundamental beams at 45° with 0 walk- off parameter and 0° Gouy Angle Shift on the AMC simulation .....	48
Figure 42: Beam Intensity Profile of HG and LG second harmonic generation beams at 45° with 0 walk-off parameter and 0° Gouy Angle Shift on the AMC simulation.....	48
Figure 43: Beam Intensity Profile of HG and LG fundamental beams at 45° with .001 mm walk- off parameter and 0° Gouy Angle shift on the AMC simulation.....	49
Figure 44: Beam Intensity Profile of Beam at 45° with 0.001 mm walk-off parameter and $0.5*\pi/2$ Gouy Angle Shift on the AMC simulation.....	49
Figure 45: Beam Intensity Profile of Beam at 45° with 0.001 mm walk-off parameter and $0.25*\pi/2$ Gouy Angle Shift (Left) and $0.75*\pi/2$ Gouy Angle Shift ( Right) .....	50
Figure 46: Beam Intensity Profile of Beam at 45° with 0.001 mm walk-off parameter and $0.8*\pi/2$ Gouy Angle .....	50
Figure 47: Beam Intensity Profile of Beam at 45° with 0.001 mm walk-off parameter and $0.85*\pi/2$ Gouy Angle .....	51
Figure 48: Beam Intensity Profile of Beam at 45° with 0.001 mm walk-off parameter and $0.9*\pi/2$ Gouy Angle .....	51

# Abstract

A high-power 1310 nm VECSEL with orbital angular momentum would be very beneficial to optical communications because it would allow for orbital angular momentum to be used as a multiplexing technique, drastically increasing the bandwidth of optical communications[5]. Two main initial design parameters were investigated for the design of such a laser; material of the quantum well structure and thermal management techniques, along with other secondary design parameters. An initial assessment of the best option was given along with secondary choices depending on the circumstances. A Live ABCD Matrix Beam profile simulation program in Matlab was discussed, including the theory, how the code was made, and the inputs and outputs of this program. This program was specifically designed for the V cavity VECSEL and thus can also be used for the high-power 1310 nm VECSEL with orbital angular momentum. It can be used to have instant feedback and an increased ability to troubleshoot any issues or constraints that present themselves moving forward during the design and creation process for this VECSEL. Finally, there was an investigation into the simulation of an astigmatic mode converter at an angle to analyze whether or not this would be able to compensate for spatial walk-off. The theory of an Astigmatic Mode Converter and how to code one is investigated. Once the creation of the code had been explained, the spatial walk-off was input into the simulated beam. Lastly, the AMC's angle was incrementally changed, and results were analyzed to determine the effect on distortion.

# Table of Acronyms

AlGaAs/InP	Aluminum Gallium Arsenide/ Indium Phosphide
AMC	Astigmatic Mode Converter
DBR	Distributed Bragg Reflector
DH	Double Heterostructure
GUI	Graphic User Interface
HG	Hermite Gaussian
InGaAsP/InP	Indium Gallium Arsenide Phosphide/ Indium Phosphide
LASER	Light Amplification by Stimulated Emission Response
LG	Laguerre- Gaussian
MQW	Multi- Quantum Well
OAM	Orbital Angular Momentum
OPS	Optically Pumped Source
QW	Quantum Well
ROC	Radius of Curvature
SEASAM	Semiconductor Saturable Absorber Mirror
VCSEL	Vertical Cavity Surface Emitting Laser
VECSEL	Vertical External Cavity Surface Emitting Laser

# Chapter 1: Introduction/ Background

## 1.1 Introduction/Application

A 1310 nm VECSEL with higher-order transverse modes capabilities is the main focus of this paper. An initial intro discussing the applications of and general information of such a laser will be discussed, followed by sections investigating initial design parameters, a simulation of ABCD matrices to determine potentially viable beam parameters, and an investigation of compensating spatial walk-off in a VECSEL using an Astigmatic Mode Converter.

### 1.1.1 Importance of 1310 nm wavelength

Currently, three primary wavelengths are used in fiber optics which are 850 nm, 1310 nm, and 1550 nm[2]. These wavelengths were not chosen randomly; a collection of variables determined which wavelengths to use. These variables often fall under different constraints, including manufacturing, optical quality, and cost. As with many technologies, optical fibers started from borrowing technologies[2]. Therefore, the initial wavelength used was the one that they had the most readily available, which was 850nm [2]. The use of 850nm is an example of constraints in manufacturing and cost determining the solution. As the technology moved forward, more and more focus was on the quality of the optical properties, specifically the optical transmission of the fiber. One of the most critical transmission optical properties is attenuation[1]. Attenuation is the decrease in signal strength caused by absorption scattering and radiative loss[1]. Attenuation is measured in dB and is calculated using equation 1.

$$dB = 10 \log\left(\frac{\text{power level in } W}{W}\right) \quad (1)$$

Attenuation is dependent on wavelength when considering optical fibers, and eventually, the graph of optical loss vs. wavelength was created for silica-based optical fibers[1,2].

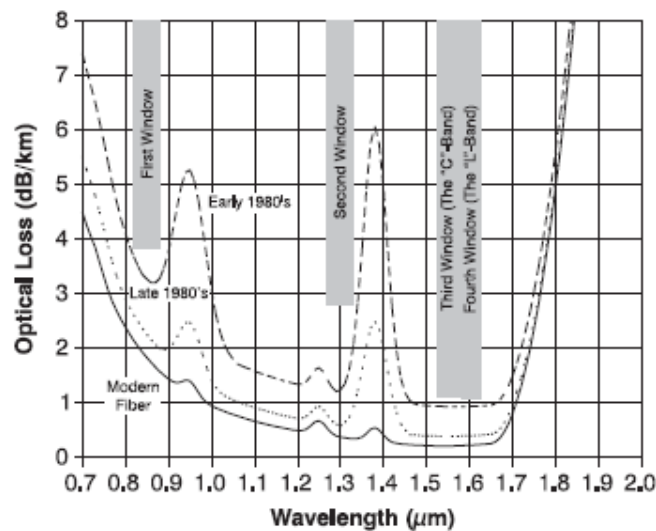
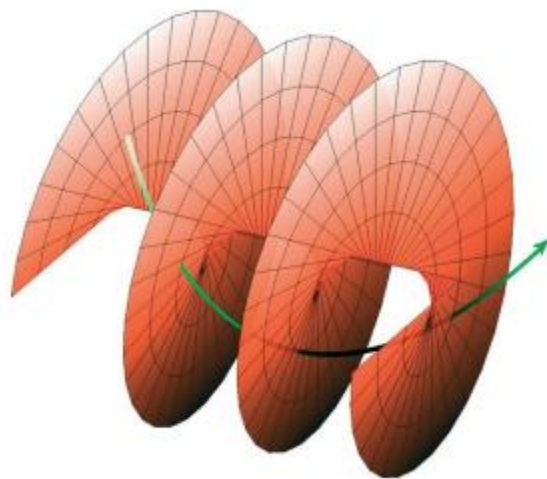


Figure 1: Optical Loss vs Wavelength 1980's to Modern times[2]

The ideal situation is to have as little loss as possible when transmitting through an optical fiber. Figure 1 highlights why specific wavelengths were chosen throughout the optical communication history[2]. Initially, when the optical loss vs. wavelength was determined, three windows would be viable for optical communication [2]. While these windows were not small enough to narrow down to specific wavelengths, other essential variables narrowed these down to the three wavelengths in use today, 850 nm, 1310nm, and 1550nm [2]. These wavelengths can be seen in Figure 1 by the dashed line labeled the Early 1980s[2]. Today, with advances in the quality of the fibers and other factors, the minimum attenuation at 1310 nm is .5dB/km, and at 1550 nm, it is .2 dB/km[1,2]. Another optical property that becomes vital at this point is dispersion[1]. Dispersion is the interference between the broadening adjacent pulses and the fiber[1]. It determines the maximum achievable data rate, thus making it the most crucial fiber characteristic after transmission loss[1]. 1310 nm is dispersion limited, whereas other wavelengths are loss limited, meaning that it is optimized for two of the most critical variables for determining wavelengths in optical communications[1]. These optimizations are why, for applications under 10 km, 1310nm is most widely used[1]. Now that the importance of the 1310 nm wavelength has been determined, orbital angular momentum will be investigated.

### 1.1.2 Orbital Angular Momentum Applications

Poynting is credited with being the first person to infer that light must have an angular momentum [3]. At the time, he was unaware that it was split into two different contributions[4]. The two contributions are spin and orbital angular momentum[4]. Spin contributions are dependent on the polarization and can be up or down, relating to  $\pm "h"$  (Planck's constant) [4]. Orbital angular momentum is phase, spatially, and polarization independent and can be a multiple of "h"[4]. This optical phenomena and these properties can be derived from Maxwell's Equations and have been proven experimentally [3,4,34].



*Figure 2: Helical wave fronts with associated Poynting Vector to produce orbital angular momentum [4]*

There are vital properties OAMs have that make them suitable for many optical fields, but the focus will be on the property that helps the most with optical communication. This property is that, theoretically, it has an unlimited number of orthogonal states [3]. The importance of this

property means that orbital angular momentum mode division multiplexing is possible[5]. Multiplexing uses techniques to encode information into optical properties such as wavelength, amplitude, phase, and polarization[5]. This technique allows more information to be sent at a time through an optical fiber or communication route by differentiating between different signals according to the changes in said optical properties[5]. Some of these multiplexing optical properties are described in Figure 3.

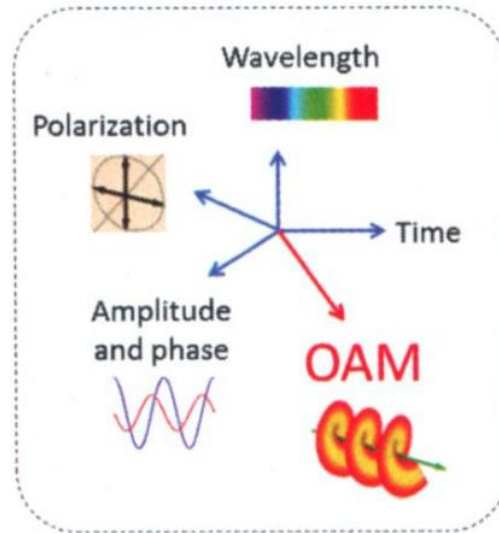


Figure 3: Common multiplexing optical properties [5]

These other optical properties are also effective at multiplexing, but they have reached max capacity due to the nonlinear effects of these properties; thus, the reason for investigating new multiplexing techniques such as OAM[5]. OAM would allow another orthogonal property to be added to current multiplexing techniques, increasing the fibers' capacity without fear of interaction between those properties. Another critical difference between OAM and other optical properties is how easy it is to encode and therefore becomes an essential feature for information where protection is critical[5]. Orbital angular momentum and wavelength division multiplexing has already succeeded in initial testing and is orthogonal to the other typical optical properties used in multiplexing, as seen in Figure 4[5].

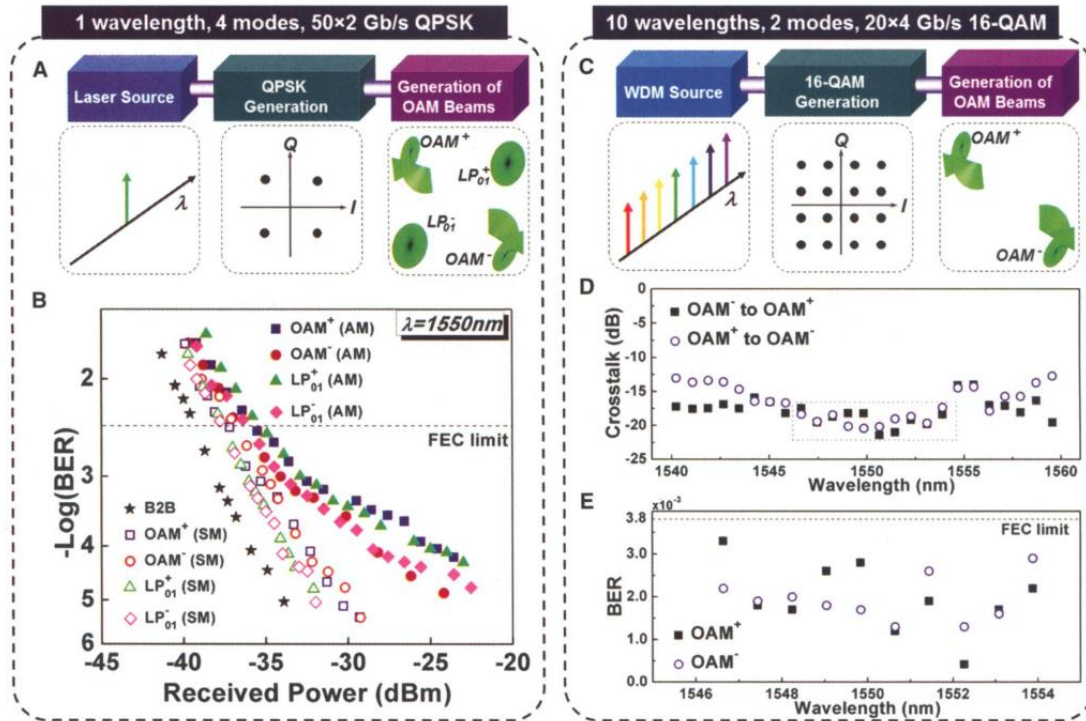


Figure 4: Crosstalk analysis of OAM with different multiplexing properties[5]

Figure 4 is from a study investigating the crosstalk of OAM with other multiplexing techniques[5]. The results show that the crosstalk is kept to an acceptable level with different wavelengths and different polarizations ( spins) [5]. These properties were chosen because they are common and are also the most likely to have crosstalk being an issue[5]. VECSELs meet the beam requirements necessary to use OAM and 1310 nm, as explained below.

## 1.2 Critical VECSEL Attributes

The Vertical External Cavity Surface Emitting Laser basics will be explored and how it helps with these optical communication applications. This section will describe the fundamental aspects of a VECSEL, the power capabilities, and Higher-Order HG/LG modes.

### 1.2.1 Basics of VECSEL

VECSELs are very similar to VCSELs (Vertical Cavity Surface Emitting Lasers). The main difference is that the cavity is external on a VECSEL compared to a VCSEL[6]. The external cavity is accomplished by replacing one of the distributed Bragg mirrors with a transparent window allowing the cavity to be outside the semiconductor[6]. A VECSEL is similar to every laser because it contains the essential components of a gain medium, a cavity, and a pump source. A benefit of VECSELs is the ability to insert more complex components in the cavity because it is external and accessible.

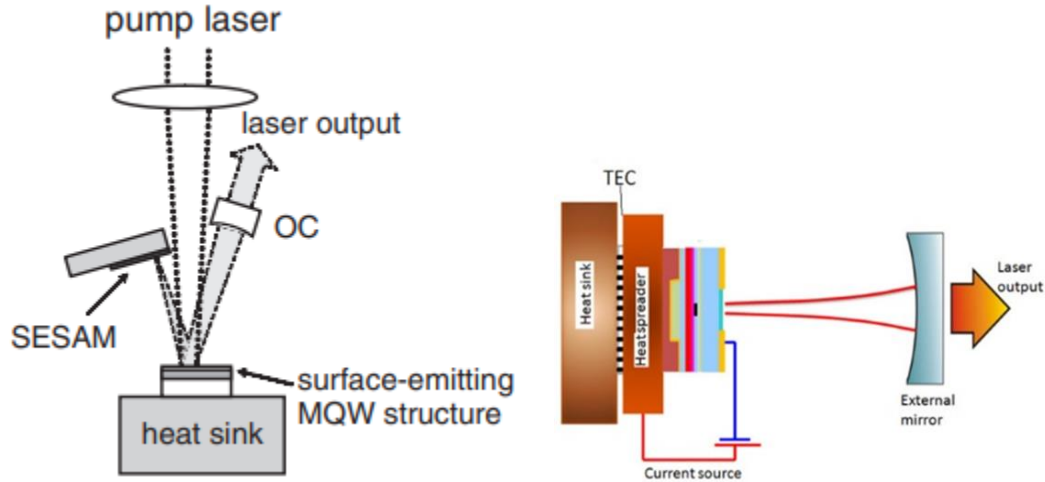


Figure 5: Two standard VECSEL Set ups, V-Cavity (LEFT) and Standard Cavity (Right) [6]

Figure 5 is a standard configuration of a VECSEL and allows for the investigation of the standard components of a laser[6]. Firstly, every laser starts with a pump, which "starts" the laser by exciting the gain medium. The two most common pumps are electrically pumped and optically pumped[36]. OPS or optically pumped semiconductor VECSELs are much more common recently because they avoid some of the restrictions of VCSELs which have similar beam characteristics to electrically pumped VCSELs[36].

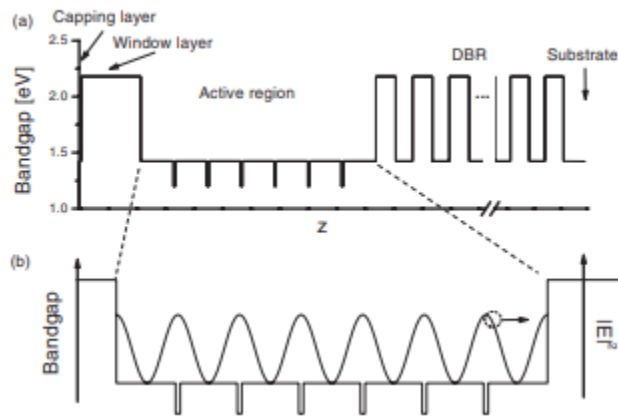


Figure 6: Multi-Quantum Well Active Region Semiconductor Structure[6]

The gain element in a VECSEL is grown on a semiconductor structure. The gain element is the material that will produce the laser through the pump by being excited into higher states. Figure 6 is a model of the semiconductor structure[6]. The active region depicted in Figure 6 is a periodic array of Quantum Wells spaced at  $\frac{\lambda}{2}$ [6].

Surrounding the gain region or active region is the last component required in laser operation: a cavity or optical resonator which contains the gain medium and ensures that the laser light

continues to operate. It is shown that there is a distributed Bragg reflector (DBR ) mirror on one side of the active region[6]. On the other side, a window allows it to leave the semiconductor structure, thus creating the external cavity[6]. Once it leaves the semiconductor, the shape of the cavity will determine how many more mirrors it will hit before it returns to the semiconductor[6]. In Figure 5, a V cavity is on the left, and a standard cavity is on the right. The application of the VECSEL determines the best shape to be used, including adding a leg of the cavity for the Semiconductor saturable absorber mirror ( SEASAMS) or nonlinear crystal such as frequency doubling crystal[6].

Besides the most critical features, there is also the cooling system of the VECSELS. These are important due to the thermal sensitivity that VECSELS suffer from because they are quantum well lasers [6]. Generally, there is a shift of  $0.3nm K^{-1}$  with respect to temperature, and this shift needs to be accommodated when designing these lasers[6]. The thermal shift or redshift requires good thermal management, and thus underneath the semiconductor, there is a heat sink. Many heat sinks can be used, but this will be discussed during the thermal management literature review.

The main advantages and reasons for using a VECSEL are the beam conditions and properties that can be made from one. Specifically, it can make OAM beams with higher-order HG/LG transverse modes and power capabilities.

### 1.2.2 VECSEL Power Capabilities

Due to transmission losses, detector sensitivity, and other losses in optical communications, it is necessary to get at least a couple of watts of power from the laser source used for these applications. This power requirement is one of the reasons that VECSELS were chosen as a potential source for this type of optical communication. Many examples of VECSELS have power between 2W and 6 W with various cavities, materials, and wavelengths[8,9,10,11]. This versatility in variety and capability to reach those high powers is one of the reasons that this laser is considered for optical communications [8,9,10,11]. While this versatility is good, it was also essential to know if it would work for the specific needed restrictions of the application. Figure 7 shows the wavelengths one study on VECSELS could accomplish by tuning the wavelength and keeping the power[8]. Figure 8 shows the same study's data and the powers they could pull in different HG/LG modes and at different wavelengths[8]. This versatility in high power with other properties being able to change shows that VECSELS are a viable solution for high power higher-order OAM 1310nm beams. The importance of LG (Laguerre Gaussian) modes in OAM will be discussed shortly.

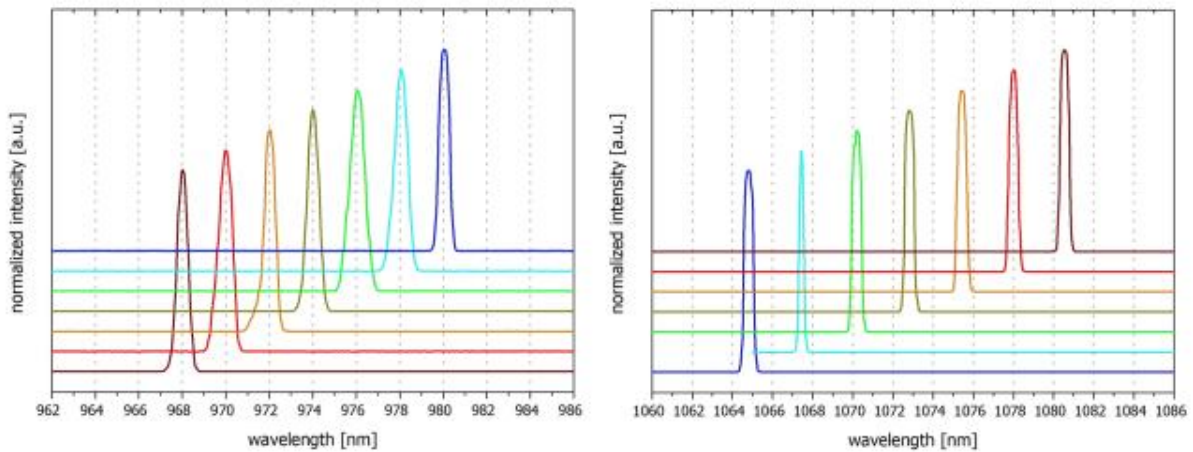


Figure 7: The Tuning Spectra of a set of VECSELs [8]

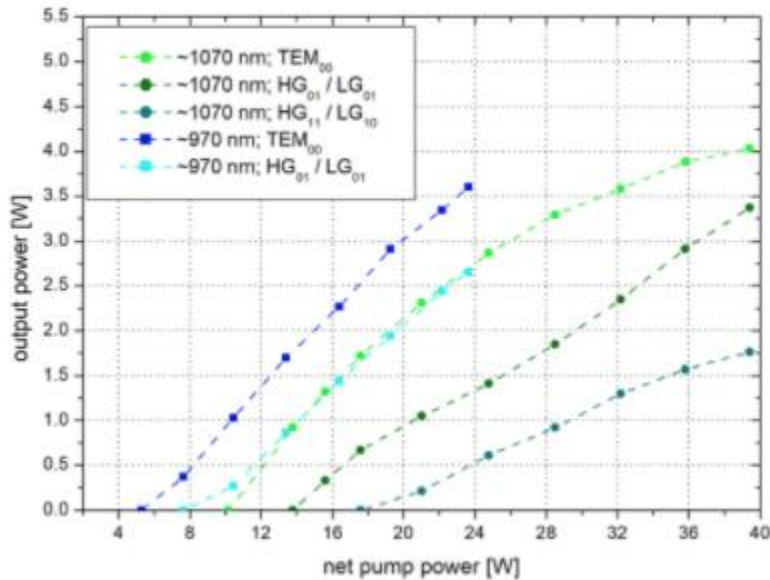


Figure 8: Output Power[W] vs net pump power[W] of a VECSEL operating at different Hermite- Gaussian and Laguerre Gaussian Transverse modes [8]

### 1.2.3 Higher Transverse Mode Beams/Laguerre Gaussian Beams

Laguerre Gaussian Beams( LG) are Gaussian beams with beam profiles that mathematically solve the Helmholtz equation using Laguerre polynomials[12,24]. These beam profiles are described as modes, and an essential feature of LG beams is that they possess an orbital angular momentum of  $l * h$  per photon[24]. The name Laguerre comes from using Laguerre polynomials to solve the Helmholtz equation[12]. These phases are described using the indices "l" and "p" [12]. "l" or azimuthal angle determines the ring size of the fundamental beam, shape of the pattern, and the helicity of the beam[12]. "p" or radial quantum number determines the number of dark rings or radial nodes tare found in the beam profile. Figure 9 shows the beam profile of different indices of LG modes[12].

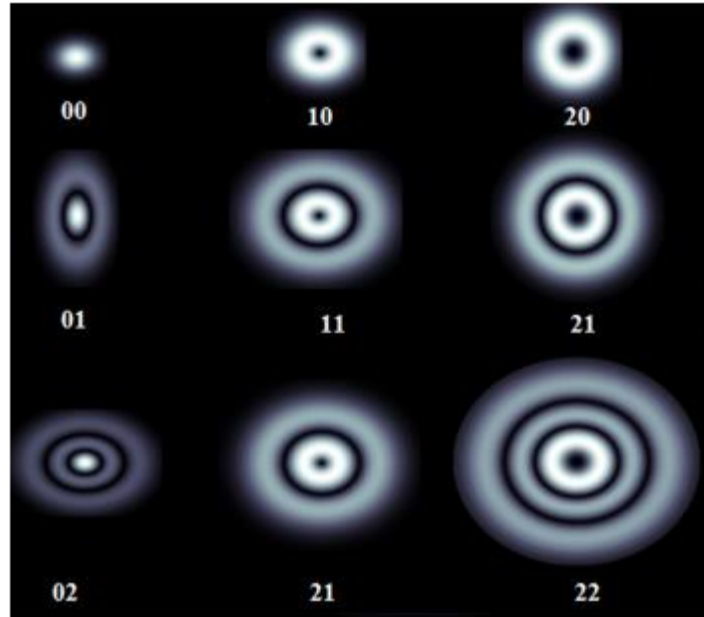


Figure 9: Different beam profiles of LG modes[12]

The importance of the LG mode beams is that they are one of the easiest ways to allow for the creation and usage of OAM. With VECSELS, it has already been shown that higher-order LG beams can be produced with high power and high quality[38]. This capability is one of the final pieces that indicate the benefit of using VECSEL for research into OAM optical communication[7]. Figure 10 shows the results of a study that was able to do this. [7].

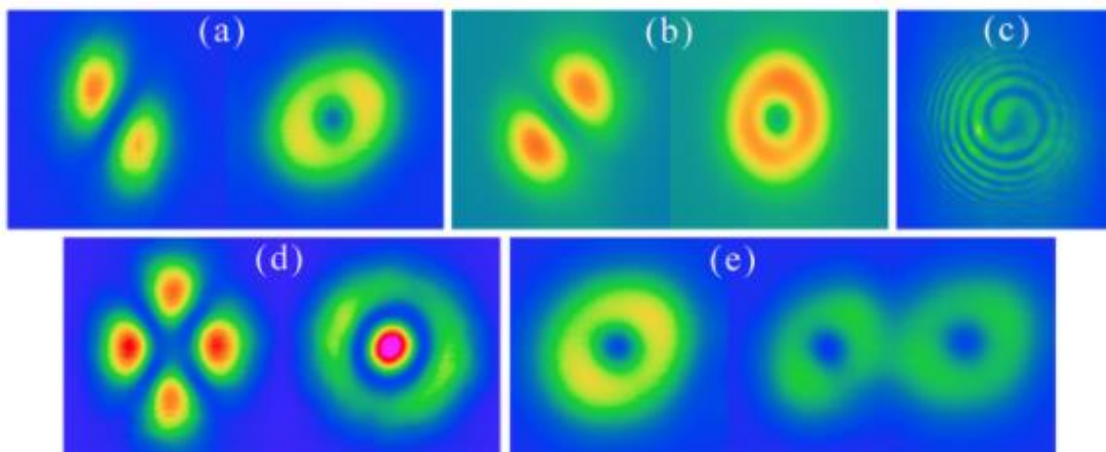


Figure 10: Experimental Beam Profile results of VECSEL's of LG Beams [7]

### 1.3 Conclusion

In conclusion, investigating VECSELS that operate at high power and 1310nm is critical because of the long-term applications of these lasers. This laser method gives many options for creating

the signals needed for OAM multiplexing and other applications. The purpose of this thesis is the initial design of a laser that accomplishes the parameters necessary to allow for OAM multiplexing. The first section is a literature review to determine the design of the semiconductor structure, including materials and thermal management options, and other vital features. Following that, a simulation tool will be shown to help determine beam cavity parameters that can be used later in developing this VECSEL. Lastly, using an Astigmatic Mode Converter to compensate for spatial walk-off will be simulated and tested.

## Chapter 2: Initial Literature Review of Design of 1310 nm VECSEL

### 2.1 Introduction

Whenever the design of any laser is begun, it is crucial to understand the basic structure and mechanisms that are key to this type of laser. In the intro section, the essential components of a VECSEL were explained. The literature review section will focus on critical design properties and decisions that would most efficiently accomplish the previously-mentioned OAM optical communication goal. These properties include but are not limited to thermal management, Distributed Bragg reflectors(DBR), and the multi-quantum well (MQW) semiconductor structure materials. This introduction will dive deeper into the mechanisms of the MQW structure that need to be understood.

For the more complex topics of a VECSEL, an understanding of the basic functionality is required. Previously, it was mentioned that a laser has three main components: gain medium, pump source, and resonators. The gain medium in a VECSEL can use MQW to optimize specific beam parameters. The pump source is either an electronic connection or another laser connected to or directed at the gain medium[24]. The optical resonators include the DBR and external coupler mirror, which is not 100% reflective, so there is an output for the laser. The space between the output coupler mirror and the DBR defines the external cavity. The typical laser mechanism is that the pump starts to excite the gain medium into higher states[24]. When the molecules return to their previous state, they emit light that is the desired wavelength through spontaneous or stimulated emission; these will continue interacting with other molecules in the gain medium[24]. These interactions will continue until more molecules are excited rather than in the lower normal state. When this occurs, it is called population inversion, and this is necessary to be lase[24]. It is required to lase because once this state has been achieved, the emission of photons will be higher than the loss of photons[24]. The cavity and resonators are critical because the light needs to be redirected back into the gain medium for the population inversion [24].

The surface-emitting semiconductor gain medium is a topic that has been researched extensively. Firstly, due to requiring a bandgap, the chosen materials usually include a combination of third and fifth group materials in the periodic table[13]. The basics of any semiconductor laser material choice are centered around the bandgap. The bandgap is the difference between the

valence band's top energy potential and the conduction band's bottom energy potential [13]. A specific energy value determines this bandgap; this energy value will determine the wavelength of the emitted light [13]. The energy value is calculated by " $h * \nu$ " where " $\nu$ " is the inverse of wavelength and " $h$ " is Planck's constant [13]. This formula and theory is depicted below in Figure 11. [13].

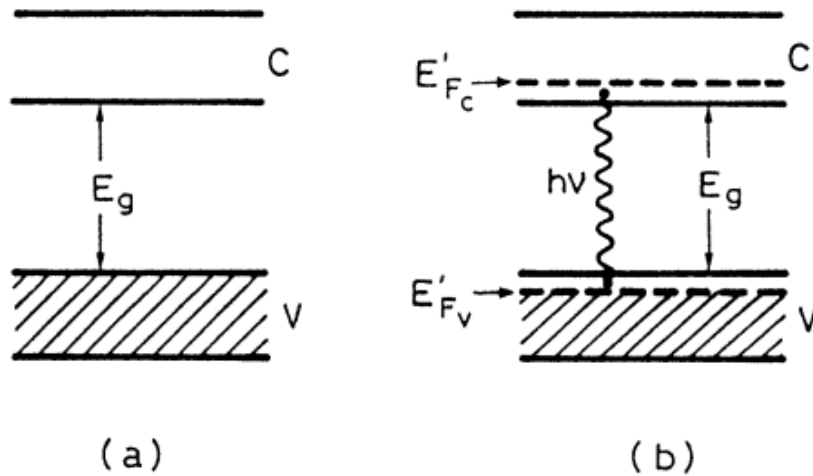


Figure 11: Principle of operation of a semiconductor laser [13]

Light interacting with the semiconductor gain medium allows the material to start lasing at the correct wavelength. However, more is required for it to sustain this. Population inversion in semiconductor lasers can be described as having more molecules in the conduction band than the valence band. It is required to guarantee that there will be enough light and interactions [13]. As was mentioned previously, population inversion is necessary to lase, and when population occurs, the gain medium can now be defined as active material [13]. Population inversion is accomplished by spontaneous emission, stimulated emission, and absorption which are shown in Figure 12 [13].

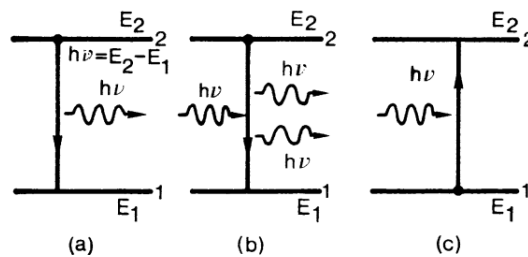


Figure 12: Schematic illustrations of spontaneous emission (a), stimulated emission (b) and absorption (c) [13]

Population inversion ensures that there will be a large number of these interactions, leading to an amplification effect which is where Light Amplification by Stimulated Emission (

LASER) is derived. [13]. The most important aspect is that these interactions have more gain (amplification) than loss; if this is accomplished, lasing will occur[13]. Population inversion is supplemented by the proper combination of P-doped and N-doped materials, which allows for more holes and extra electrons[13]. These additional holes and electrons assist by altering the bandgap and other properties to allow population inversion more readily[13]. These factors lead to the most common structure of semiconductor lasers and are called the Double Heterostructure Laser and are partially used in VECSELs[13]. The diagram for that laser is pictured in the Figure 13.

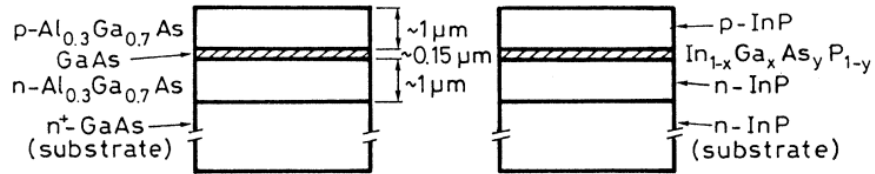


Figure 13: Diagram of double heterostructure laser [13]

The shaded regions in Figure 13 indicate the active region[13]. The structure and placement of the materials assist in the lasing capabilities of this semiconductor laser through the index of refraction, bandgap, and location of the extra holes and electrons [13]. One important note is that the lattice structure of the three regions needs to be within 0.1% of each other[13]. The lattice structure is defined by the lattice constant, which is the value that must be within 0.1% [13]. Otherwise, there is potential for strain on the interface, which will cause misfit dislocations which cause unwanted electron-hole nonradiative recombination, increasing losses [13].

If the active layer is reduced in thickness to be comparable to the de- Broglie wavelength, this is a quantum well; when many of these are placed in a row, it is the multiple quantum wells version of the DH laser[13]. The positives of MQWs are increased differential gain and decreased dependence of this gain on temperature, which is caused by the entirely different density states of QW material vs. bulk material[13]. A con of this method is that this also reduces the confinement factor due to reduced layer thickness, requiring a separate confinement structure [13]. The separate confinement structure ensures that the beam is confined to the correct area of the gain in the semiconductor[13]. A simple example of MQW and its confinement structure is shown in Figure 14 and Figure 15; this is similar to how it is applied in a VECSEL[13].

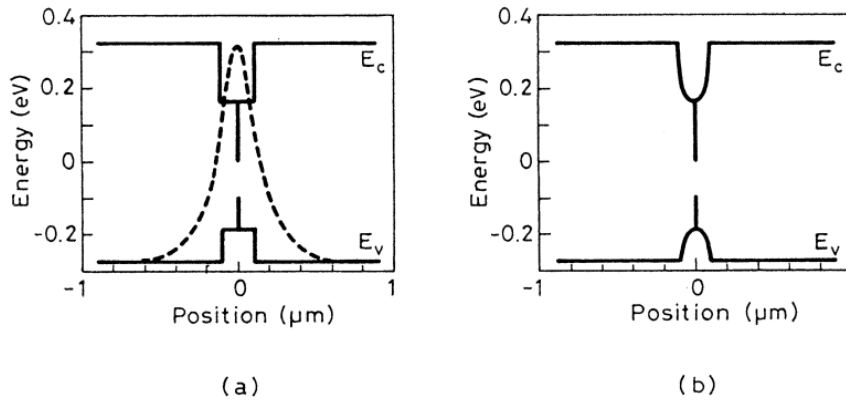


Figure 14: A diagram of a single quantum well heterostructure depicting the energy band versus position [13]

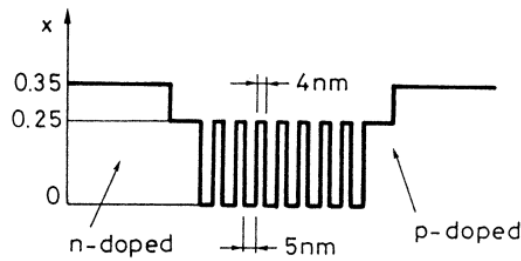


Figure 15: Diagram of MQW [13]

One other important note about MQW is that the strain becomes less critical. Therefore, differences in the lattice structure up to 1-3% can be tolerated, allowing or broadening the possible wavelengths that can be created due to increased bandgap [13].

Figure 16 shows the use of all these theories in a VCSEL (a VECSEL without the external cavity) [7,13].

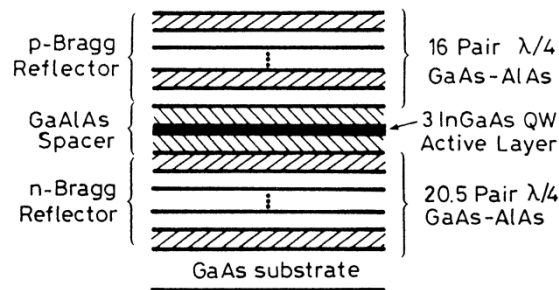


Figure 16: Diagram of VCSEL Structure [13]

It is common in most semiconductor lasers to have a high dependence on temperature for wavelength [14]. The redshift is the gain peak wavelength moving toward longer wavelengths, resulting in bandgap narrowing due to higher injection levels [14]. There is a blue shift with the peak gain wavelength going to shorter wavelengths, resulting from a band filling effect [14]. In most cases with semiconductor lasers, the bandgap narrowing is more prominent; therefore, there

is usually a redshift when the temperature is increased[14]. Typically this temperature dependence is written as equation 2 for simplicity[14].

$$I_{th} \propto e^{\frac{T}{T_0}} \quad (2)$$

This redshift is one of the many reasons that thermal management in the next section is critical to designing these lasers.

## 2.2 Thermal management

With the importance of thermal management, there have been many ways developed to contain and control the heat emitted on the semiconductor structure. Two methods are being investigated Ti/Au/In Flip Chip bonding of diamond or intracavity diamond. The pros and cons of each will be assessed separately and when using both simultaneously.

In its simplest form, the difference between an intracavity diamond heat spreader and a flip-chip diamond heat spreader is whether it is in the cavity or outside of it[9]. This difference is highlighted in Figure 17[9].

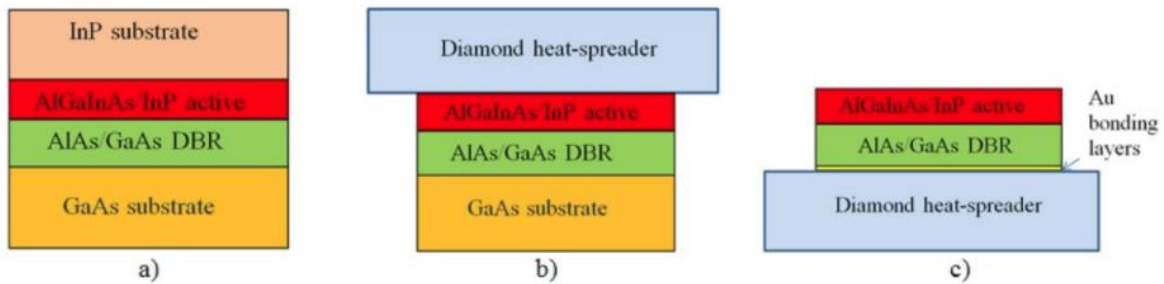


Figure 17: Diagrams of fused gain mirror stack (a), intra-cavity diamond (b), and a flip-chip(c) thermal management methods[9]

The pros and cons of using these methods become more evident after seeing how they are integrated into the chip. Flip-chip has the significant benefit of being outside the beam; therefore, it introduces no optical distortions or aberrations[15]. In situations where specific beam parameters are critical, this option becomes much harder to implement and most likely has to deal with an increase in the cavity losses regardless of application [15]. On the other hand, the actual assembly of the intracavity diamond heater seems much more straightforward, requiring that alcohol or water is used to capillary bond the diamond to the as-grown structure and be held in place by a constant mechanical pressure[15]. Flip-chip is a more permanent bond that includes chemical vapor deposition heat spreaders while balancing and protecting the assembly from excessive heat during installation[15]. On top of all this, this method requires that the entire semiconductor structure be built upside down to give access to the DBR mirrors to which the diamond heat spreader will be permanently bonded [10].

The actual comparison of heat dissipation has been done in several ways between the two methods. Currently, multiple studies seem to be indicating the same analysis, intracavity is better currently, but flip-chip has been making progress in recent years that has made the difference between the two much smaller[11,15,37]. Figure 18 summarizes this data for one of the studies[37].

Approach to thermal management	Diagram	Location of diamond	Max. temperature rise per unit pump power ( $KW^{-1}$ )	
			0.98 $\mu m$ device	2.35 $\mu m$ device
"As grown"	Figure 11.4a	No diamond	21	86
Thinned, diamond sub-mount	Figure 11.4b	Extracavity	2.7	26
Diamond heat spreader	Figure 11.4c	Intracavity	2.1	4.6

Figure 18: Results from a study investigating the different thermal management methods and capabilities [37]

This study shows that currently, the intracavity performed better by keeping the max temperature lower[37]. However, another critical feature is that this difference between the two methods was significantly different with the different pump sizes, and this is not the only variable that changes the effect of the thermal management method[37].

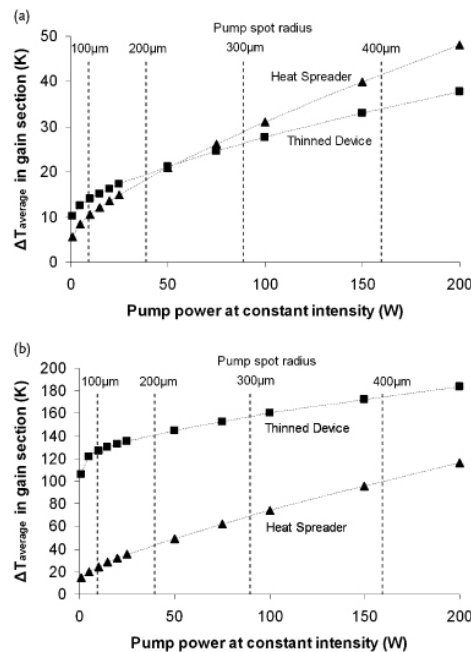


Figure 19: Shows the average temperature rise in gain section versus pump power, with the first graph being 0.98  $\mu m$  disk laser and the second graph showing a 2.35  $\mu m$  disk laser [37]

The different effects of pump power and size were investigated further in the Figure 19[37]. The different movement of the thermal load is what causes the difference between these two methods, and that is what causes the correlation between the thickness of the VECSEL and pump power[37]. Therefore, when choosing between the two, it is crucial to keep this in mind[37].

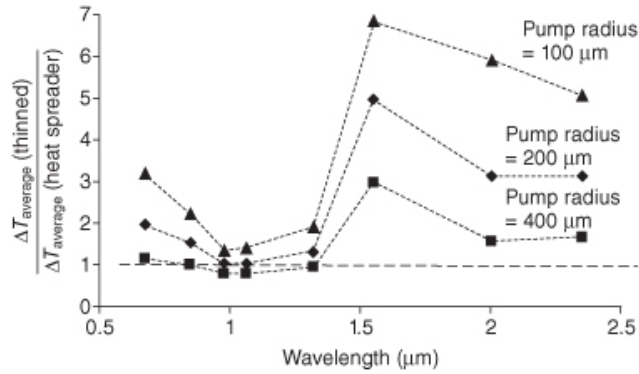


Figure 20: Ratio of temperature in the heat spreader and thinned devices for different wavelengths with different semiconductor materials systems[37]

To help with the dilemma of the complex correlation of these variables with these two methods, Figure 20 shows the simulation of the different rise of temperatures between the two methods at standard pump radii and wavelengths found in the literature[37]. The Y-axis is the ratio of the flip-chip rise in temperature over the intracavity rise in temperature[37]. Essential for this paper is the 1.3 μm region. At 1.3 μm, it can be seen that the intracavity does perform better; however, it has been mentioned in multiple studies that recent improvements have made the flip-chip more and more effective in closing the gap between the two[9,15,37]. Taking the thermal dissipation quality of each method is a critical step. However, other factors, including the intracavity method's beam effect and the flip-chip method's temperature dependence, also need to be considered[9,15].

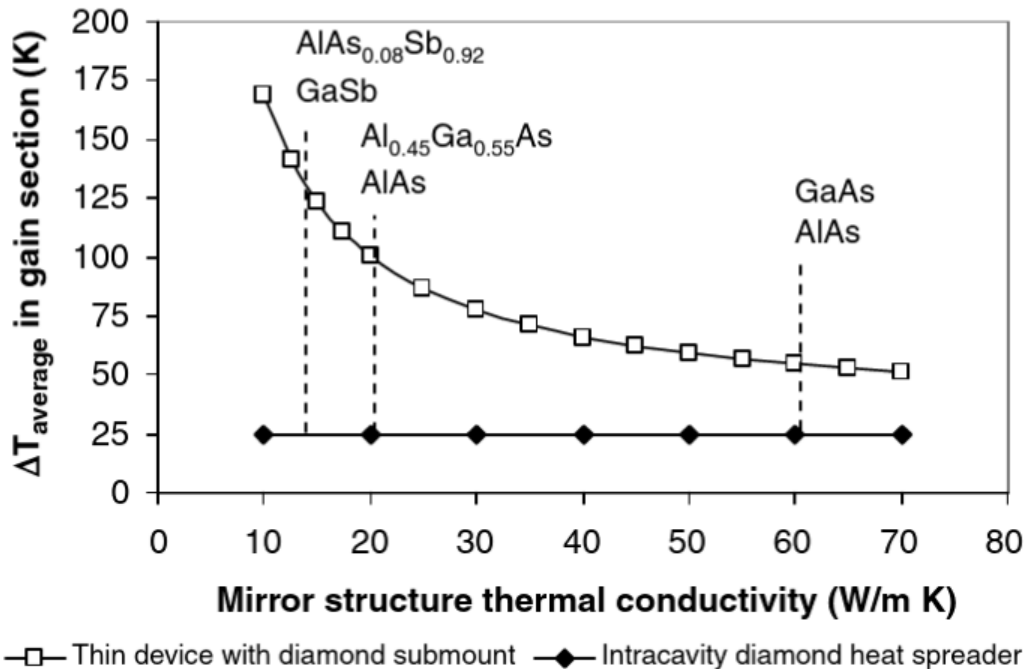


Figure 21: Flip-Chip(thin device with diamond sub mount) vs Intracavity average temperature change in gain section [27]

The dependency of the flip-chip method on the temperature is shown in Figure 21[27]. This dependency is a negative effect worth considering because of the redshift, which will be discussed next, and the DBR window, which will be discussed in the next section[27].

Determining the redshift that can be expected with different VECSEL sets up is essential. When determining the material to be used, the band gap becomes vital in determining the wavelength. It can be challenging to get the materials choices correct without an estimate on the expected shift or the shift versus wavelength. While the redshift is more inherent in the gain of the material rather than the choice of cooler, it is essential to note it at this point so that it can help to determine which of the cooling processes to use.

A study on the VECSEL Gain characterization determined that the red shift is typically between  $0.15 - 0.18 \frac{nm}{K}$ [16]. This information matches an older source suggesting that quantum well lasers operate at  $.3nm/K$ , and a more recent source suggests that it operates at  $0.22 \frac{nm}{K}$  [9,10]. This data does not precisely replicate the current VECSEL being investigated, but it gives a rough estimate of the expected number. It allows for the investigation into the difference in the capabilities of heat spreaders and determines how much shift should be expected when choosing the materials.

Another possible option is using both of these methods simultaneously, called bidirectional heat dissipation[11]. When this is chosen, it means that the pros and cons of each of the methods are melded together. There is an optical beam issue due to the intracavity diamond, and the manufacturing of this part is much more complex. On the other hand, heat dissipation is much higher than achievable using only one of the methods[11].

The method that should be used to design these parts will depend on specific variables, specifically cost, that can not be determined in the initial design investigation. Therefore, different possible scenarios will be discussed with which method could be the best fit. If looking at only thermal dissipation performance, doing a bidirectional heat spreader by combining the two methods is the way that will guarantee the most heat dissipation[11]. However, this is the most expensive option because it requires both manufacturing difficulties simultaneously [11]. Another con of this method is that there is a risk that the optical distortion caused by the intracavity design will cause issues for the LG order and other beam parameters that need to be controlled[15]. There is a solution using wedged diamonds that has been implemented in some studies, but it is potentially expensive, increasing the cost even more[15]. Suppose the cost of bidirectional is too much. In that case, there are indicators that the intracavity heat spreader is more effective at heat dissipation[35]. However, once again, the effect of having it intracavity could provide too much risk [37]. An important note is that there was a disagreement on the effect of the intracavity method, potentially adding a Fabry Perot Etalon into the cavity, with one saying it would cause additional losses and one saying that it allows for better control of the wavelength[15,37]. If this risk, uncertainty, or cost is too much, then the choice goes to the flip-chip. The Flip-Chip appears to be the most risk-free and general ideal choice for this application due to the minor increase in dissipation seen around the  $1.3 \mu m$  range.

### 2.3 DBR ( Distributed Bragg Reflector)

A DBR is a distributed Bragg Reflector called a Bragg Mirror or quarter-wave stack in some applications[25]. A DBR consists of a quarter-wave stack which means that it is different materials with different indexes of refraction that have thicknesses equal to roughly  $\frac{1}{4}$  the wavelength of the light that is hoping to be reflected[25]. Equation 3 must be fulfilled to be a quarter-wave stack.

$$n_1 d_1 = n_2 d_2 = \frac{\lambda_0}{4} = \frac{\pi c}{2 \omega_0} \quad (3)$$

It is essential to have this thickness because the Fresnel reflection off of each of the stacks will reflect, and then due to the quarter wavelength in both directions, it will be half-wavelength which is a pi shift in the wavelength [24,25]. This pi shift then allows for the constructive interference of the light as it goes through these stacks [24,25]. The effect that this type of reflector has is that it is 99.999% reflective and is only reflective for specific wavelengths[24,25]. This reflectivity and wavelength dependence is key to lasers because the transmission through the non-output mirror is the loss that is working against the gain of the laser[24,25]. Lasers are usually monochromatic; this mirror acts as a filter to help with this process [24,25].

The DBR also contributes to the thermal properties of the VECSEL; just like every component in these systems, it is essential to determine and understand the thermal properties. Due to the heat source not being in the DBR and it being between the source of heat and the thermal management subsystem, the main thermal property to investigate is the DBR's effective longitudinal and lateral thermal conductivities[27]. The way to determine the thermal conductivities of these materials is shown below in equation 4 and 5.

$$k_l = \frac{\sum_i t_i}{\sum_i \left(\frac{t_i}{k_i}\right)} \quad (4)$$

$$k_r = \frac{\sum_i \left(\frac{t_i}{k_i}\right)}{\sum_i (t_i)} \quad (5)$$

Figure 22 shows standard parameters for these DBRs.

Wavelength of operation	Mirror compositions	$p$	$N$	$\Delta\lambda$ (nm)	Total mirror thickness ( $\mu\text{m}$ )	$k_r$	$k_l$	References
390	SiO <sub>2</sub> /HfO <sub>2</sub>	0.7318	11.5	77.2	1.263	1.5	1.5	[101]
670	AlAs/Al <sub>0.45</sub> Ga <sub>0.55</sub> As	0.8835	40	52.8	4.08	53.7	20.5	[56]
850	AlAs/Al <sub>0.2</sub> Ga <sub>0.8</sub> As	0.860	30	81.1	3.97	56.0	26.6	[30]
940	AlAs/GaAs	0.8839	25.5	108.5	3.64	69.9	61.4	[78]
1060	AlAs/GaAs	0.8840	25.5	114	4.1	69.8	61.2	[78]
1220	AlAs/GaAs	0.8505	25.5	125.6	4.83	69.7	61.2	[59]
1310	AlAs/GaAs	0.8528	25.5	132.6	5.21	69.7	61.2	[35]
1550	In <sub>0.18</sub> Ga <sub>0.82</sub> As <sub>0.4</sub> P <sub>0.6</sub> /InP	0.9545	48	45.9	11.47	37.9	11.8	[103]
2000	AlAsSb <sub>0.08</sub> /GaSb	0.8021	21.5	280.2	5.95	20.1	14.3	[104]
5000	Pb <sub>0.93</sub> Eu <sub>0.07</sub> Te/BaF <sub>2</sub>	0.2804	2.5	2287	2.80	9.2	1.4	[65]

Figure 22: Table of Distributed Bragg reflector materials and properties [27]

The standard material for this wavelength is AlAs/GaAs, with a total mirror thickness of 11.47 $\mu\text{m}$ , a longitudinal thermal conductivity of 69.7, and a lateral thermal conductivity of 11.8[27]. This material was selected, due to how standard it is for this wavelength in VECSELS [7,8,9,11,15,31]. Further intricacies and design of the DBR is left for future steps, as the DBR is heavily dependent on other optical properties of the VECSEL and other parameters of the VECSEL that have not been determined as of yet.

#### 2.4 Gain Medium Multi Quantum Well Material Evaluation

Two primary materials have successfully created the VECSELS with the power and wavelength necessary: InGaAsP/InP and AlGaAs/InP[17]. These materials relate to the active region of the material, i.e., the quantum wells and the cladding around them. The nomenclature indicates the first part is the quantum wells and the second part is the cladding; for example, in InGaAsP/InP, InGaAsP is the quantum wells, and the cladding is InP. When initially choosing materials, it is essential to find something that allows a bandgap and, therefore, that limits the original materials that need to be investigated. The considerations taken into account are the band gap ( which determines the wavelength created), the index of refraction, the lattice constant, and its thermal properties. These properties are affected by the composition of the material. The composition (or percentages of each of the different molecules) in these materials will be determined, along with which composition will provide the best properties. Once that is determined, the final compositions will be compared and evaluated for how well they fit this application.

For these two materials, the band gap range needed to be near 1310nm ( including deviation from redshift). The correct variation in the percentages of the molecule to achieve a 1310 nm bandgap needs to be determined. Figure 23 shows some options and why these two were possibilities for this application.

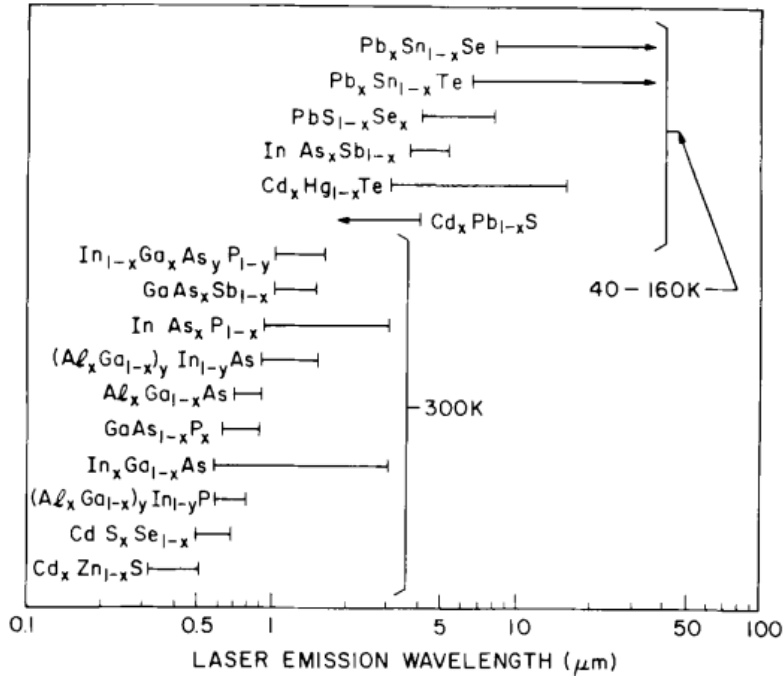


Figure 23: Emission Wavelengths of selected III -V and IV-VI compounds at 300k [17]

In Figure 23, the measurement of the possible bandgaps shown is at 300 K [17]. The first thing to notice is that several materials cover the wavelength that is being investigated. Later in the analysis, these materials' properties will make them ineligible, so the focus will be on  $In_{1-x}Ga_xAs_yP_{1-y}$  and  $(Al_xGa_{1-x})_yIn_{1-y}As$ [17].  $In_{1-x}Ga_xAs_yP_{1-y}$  has a wavelength range that goes from  $\sim 1\mu m - \sim 1.4\mu m$  while  $(Al_xGa_{1-x})_yIn_{1-y}As$  is a similar range but slightly smaller so closer to  $\sim .9\mu m - 1.3\mu m$ [13]. Both of these should be able to produce the wavelengths we are looking for, so now, we will look into what composition will work the best.

As InGaAsP/InP is more commonly used for this purpose and the information to determine which composition was much more readily available, this will be investigated first. The process of determining the x and y will be expressed for understanding and ability to compare to the other material. X and y are related to the variables in this equation  $In_{1-x}Ga_xAs_yP_{1-y}$ . Two dimensions are being solved: band gap and lattice constant. Figure 24 shows the bandgap of these parts' possible compositions.

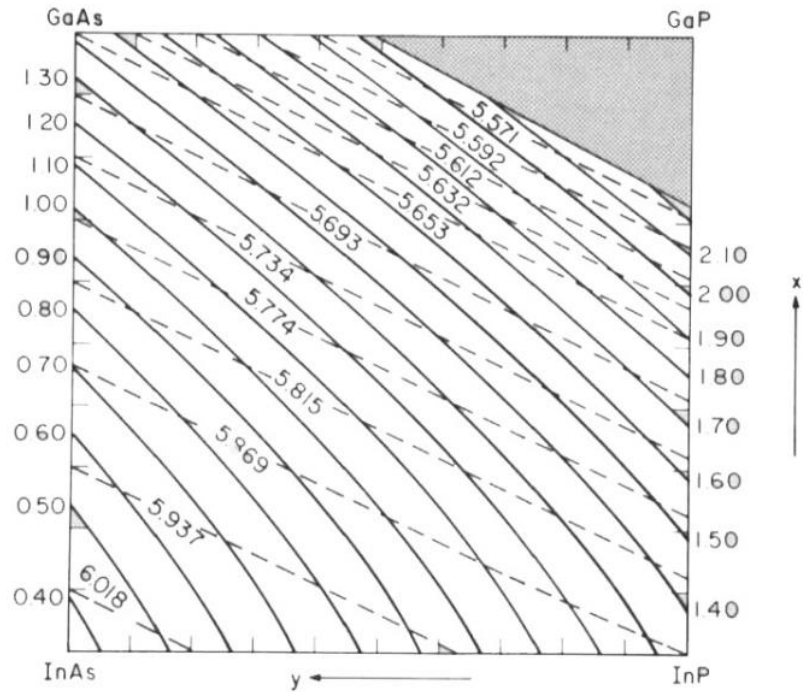


Figure 24: Composition diagram of  $In_{1-x}Ga_xAs_yP_{1-y}$  [17]

Every corner of the above chart represents 100% of the corresponding materials while the other corresponding materials are 0%. Moving along the axis, the percentage of the material in the closest corner decreases, and the percentage of the material in the opposite corner increases. The dashed lines represent iso lattice constant lines, and the isoband gap lines are shown by the solid lines. Lattice constant and bandgap are the variables being solved for; the composition is what is being determined. The bandgap is determined by dividing  $1.24/\text{wavelength}$ ; when  $1.310 \mu\text{m}$  is input, the answer is 0.946[17]. When looking at the values above, that means roughly halfway in between the solid lines labeled 0.9 and 1. Now the lattice constant needs to determine the x and y value that coordinate accordingly. As previously defined, if the lattice constant is too different (greater than 0.1% in non-quantum well and 1-3% in quantum well semiconductor lasers) in the combination of materials, then there will be strain on the material that will cause deterioration of its gain capabilities[27]. Figure 25 shows the lattice constant for InP.

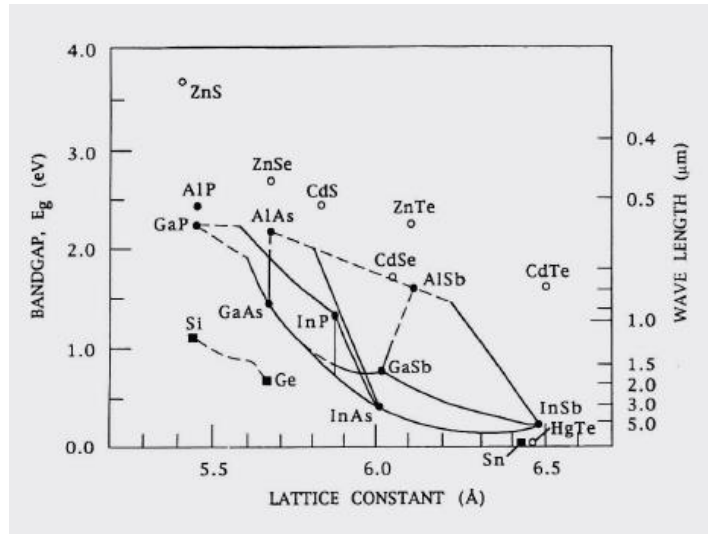


Figure 25: Energy bandgap versus lattice constant[18]

It is roughly 5.86 Å[18]. Using the banded lines, the closest one is 5.869[17]. By meeting the two of those together, it is determined to be something around  $x=0.2$  and  $y=0.5$ . This method was not the most accurate way, but it helps solidify the reasoning for verifying correct composition, and it is close to the most common composition, which is  $x=0.26$  and  $y=0.4$  or  $In_{0.74}Ga_{0.26}As_{0.4}P_{0.6}$  [17]. This solution can also be seen when plotting the iso lattice constant for  $y$  with the equation 8.

$$E_g(\text{Band Gap}) = 1.35 - 0.72y + 0.12y^2 \quad (6)$$

Which is also shown in Figure 26[17].

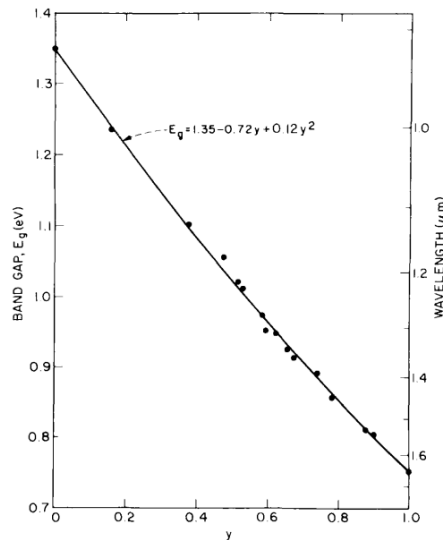


Figure 26: Bandgap composition diagram for  $In_{1-x}Ga_xAs_yP_{1-y}$  lattice matched to InP[17]

The equivalent diagram of figure 20 for AlGaInAs is shown below[19]. This one is similar to the previous one, but because As can not have a percentage attached to it, it changes the structure to be only 3 points and slightly the structure of the corners of the graph; otherwise, this is similar to Figure 27[19].

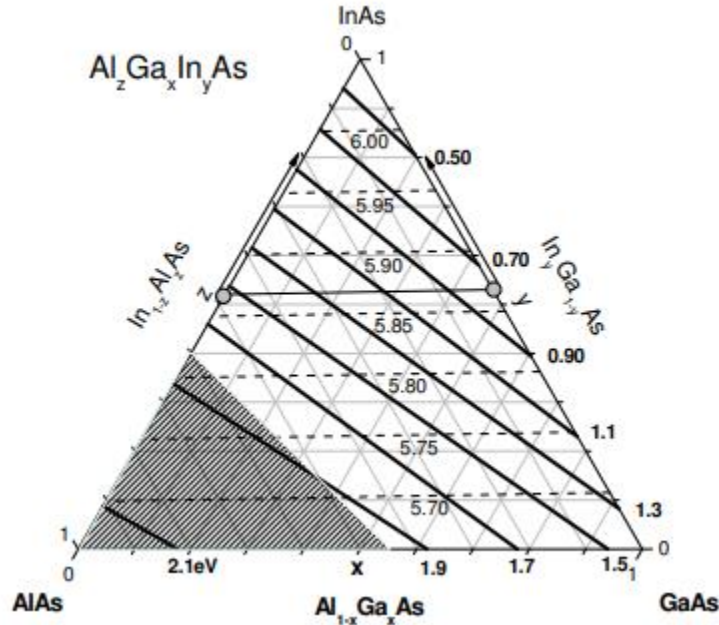


Figure 27: Lattice constant and bandgap energy of  $(Al_xGa_{1-x})_yIn_{1-y}As$  quaternary system, left bottom corner is the indirect bandgap zone[19]

From Figure 27, the lattice constant is 5.86, and from the calculation above, the bandgap desired is .946 [17,18]. Determining the acceptable range is the same process as the previous material; the dotted line at 5.85 is one dimension, and the other is a quarter of the distance between the solid 0.9 and 1.1 lines [19]. When tracking those two dimensions to an intersection, the x value is ~0.4, the y value is ~0.5, and the z value is ~0.1. Through investigation of VCSEL 1310nm studies, the value that is typically given for the composition of the quantum wells is  $Al_{.16}Ga_{.12}In_{.71}As$ [20,21,22]. This value is significantly off; however, this can come down to what is more readily available in the marketplace, other theoretical reasons not discussed here, and due to IP that is not easily accessible. Therefore, the most common composition was used because the experimental data is more compelling.

The thermal management of the gain region is similar to the situation of the DBR. The primary measurement of its thermal management is its thermal conductivity or ability to move the heat through itself and to the proper location in the system. The thermal conductivity of InGaAsP with a composition of 1.3  $\mu m$  is 0.036 W/cm/K[29]. For the AlGaInAs, the thermal resistance was 73.6 K/W which is 0.013 when changed to thermal conductivity[30]. One other aspect of AlGaInAs to consider is that when under high temperature operation, this material has reduced carrier leakage from the quantum-well region when compared to  $In_{.74}Ga_{.26}As_{.4}P_{.6}$ . [41] This is

important to thermal management because it means that this material can operate at a higher temperature before experiencing losses from the carrier leakage[41].

As mentioned before, it is vital to consider the red shift that could happen. Calculating this shift is complex because different shifts happen in the gain and cavity resonance features; therefore, thermal management is critical to reducing the risk in wavelength error[27]. Another possible way to resolve this is to make the laser slightly tunable to optimize it.

## 2.5 Conclusion

A couple of the critical components were touched on in this literature review. However, some were not discussed that are also critical, including the SEASAMs, pump laser, and other optical elements. As this is just an initial analysis, the goal was to provide initial starting data that could be used within the situation regarding cost, lead times, and other information to be determined. Next is an investigation into the capabilities shown by different sources and what was used to achieve that. The design parameters that best fit the application will be discussed.

Due to the number of variables and their dependencies, it is difficult to determine and compare the variables independently of each other. Due to this, a couple of studies will be analyzed via the whole system and its performance. This analysis will determine the optimal combinations and help narrow down the best variables/combinations.

The first study that was investigated focused on the development of the gain mirror, specifically the use of wafer bonding[8]. The highest output power accomplished was 6.6 W with a 2.5% output coupler and optical pumping of 980 nm laser at a spot size of 290  $\mu\text{m}$  at 7 degrees Celsius[8]. They used an intracavity diamond heat spreader for heat management and the wafer bonding process[8]. The wafer bonding process reduced the thermal impedance to 4K/W, which they said was a significant factor in producing 1.9 W - 2.7W at 15 Celcius[8]. The gain mirror fusion that they used for 1310 nm was the fusing of an InAlGaAs/InP active region grown on an InP substrate and AlGaAs/GaAs DBRs grown on GaAs substrates[8]. They used a standard V cavity configuration[8].

The second study continued the first, whose primary purpose was to investigate the progress made with wafer-fused VECSEL[9]. This study used the same cavity-type and similar fusion materials for the active region and the DBR, as mentioned in the previous paragraph[8,9]. A comparison was completed between the two thermal management methods intra-cavity diamond spreader and the flip-chip method[9]. 6.5W was achieved with the flip-chip gain mirrors, and 7.1 W was achieved with the intra-cavity diamond heat spreader[9]. Compared to the previous study, the cited reason for the increased wattage was replacing the multi-QW structure from 2-2-2-2 to 3-3-2-2 and increasing the residual pump reflection[9].

More studies show other VECSELs of varying power, wavelength, and other attributes but none that are as close as the work done by the studies above. Certain features of the discussed design were also not completely aligned with the design being researched in this paper, most noticeably the higher LG modes being produced. Therefore, it was decided to only look into these two designs.

As discussed before, not all of the parameters of laser have been determined, and not all of the practical variables of creating such a VECSEL are known, such as cost. With this being the case, the best fit choices will be given, considering the possible situations that could be presented in the design.

The flip-chip design seems to be the method of thermal management that takes the least amount of risk of beam issues and has similar dissipation capabilities at 1.3um[9,15,37]. The other options would be necessary if the risk of the power being limited due to lack of thermal dissipation overcame the intracavity beam risk. If the budget is restrictive in that case, the best option would be intracavity, and if it is not restricted, then the bidirectional heat spreader is the correct way forward.

The DBR material was not investigated extensively due to how often it is used for VECSELs of this wavelength, and the material is AlAs/GaAs [7,8,9,11,15,31]. The design of the DBR is also heavily dependent on other variables that have not been discussed and therefore was not investigated.

The last variable to be decided is the MQW material. This choice is of utmost importance because it is the primary gain medium of the VECSEL. The two options being investigated were InGaAsP/InP vs. AlGaInAs/InP. The investigation was done into why these two materials are the possible options, and following that, it goes into the meat of the decision. InGaAsP/InP is much more common, the wavelength range has more room for redshift around 1.3um, and the composition matches the theoretical much more closely[14,17,18,27,28]. AlGaInAs/InP potentially has a lower thermal management requirement by being able to operate at higher temperatures due to lower carrier leakage [41]. With this in mind, the InGaAsP/InP seems the right choice. It has much more data showing similar successful designs to these, and the increased range around the redshift should help offset the lower max operating temperature. The other thermal management can also be implemented if the thermal dissipation is insufficient with InGaAsP/InP and the flip-chip thermal management method.

## Chapter 3: ABCD Matrix Simulation of V Cavity Profile

### 3.1 Introduction

The cavity is where all of the lasing occurs and usually contains the entirety of the internal part of any given laser. A vital feature of the VECSEL laser is that the cavity is external, which will be discussed later. The cavity's primary function is to make the light resonate through the gain medium to create the lasing. However, there are essential requirements to keep in mind when designing a laser cavity. Firstly, the length of the cavity is very critical[24]. One of the main reasons this is critical is the coherence of the laser; coherence is where the wavelength of the laser light is in phase for space and time[13]. The cavity length must be equal to  $c/2L$ , which ensures the waves inside of the cavity are also coherent[13,24].

Other key features of laser cavities are the mirrors placed at their ends to achieve resonance. One of the mirrors will be as close as possible to 100% reflectivity to reduce loss in the cavity, while the other one will not be fully 100% so that some of the laser light gets transmitted to the laser's output. Another critical feature is resonator stability[24]. Resonator stability is determined by whether or not the photons will be confined within the cavity overtime[24]. If the light eventually escapes the cavity, it is an unstable cavity. If the light will remain indefinitely, then it is a stable cavity. Figure 29 models the difference between a stable and unstable cavity.

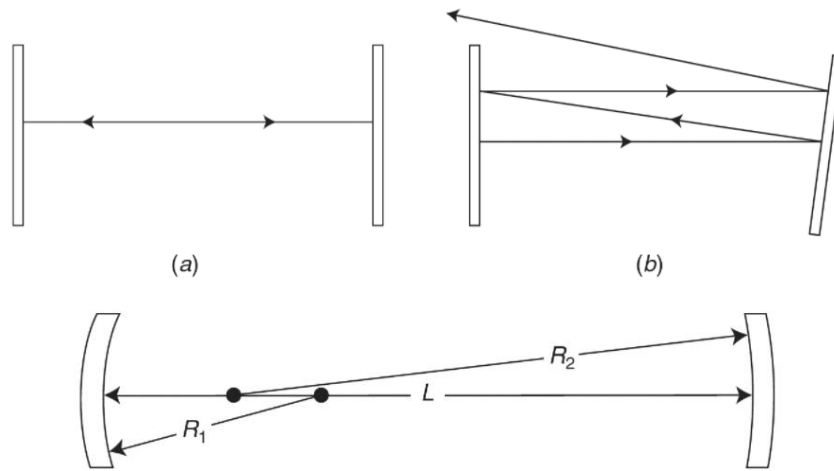


Figure 28: Different laser resonators, first with flat parallel mirrors, second flat mirrors with non-parallel mirrors and thirdly resonators with curved mirrors[24]

As shown in Figure 29 and 30, one of the ways to accomplish a stable cavity is to change the radii of the mirrors, and this will allow for the alignment of the laser to not have to be as perfect as it would need to be if two parallel mirrors were used[24]. Some lasers are purposely made to be unstable, and there are benefits to having this be the case, but this research focuses on stable resonators.

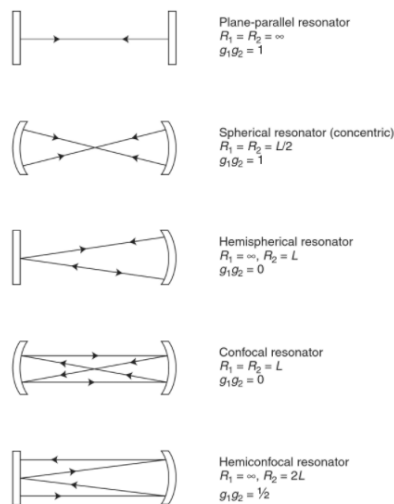


Figure 29: Examples of stable resonators[24]

Another critical aspect of the radii of these mirrors is that it will determine if other resonances are allowed in the cavity besides the indicated center perpendicular resonance. This non-center perpendicular resonance is a higher mode, which will be explained in greater detail later.

There are several benefits to VECSELs' external cavity, including the different optical devices that can be added that can change the properties of the beam. These properties include HG to LG converters, frequency doublers, and other optical devices that are difficult to incorporate into other lasers with no external cavities[6,7,8]. There are also different types of cavities, including T, W, and V cavities, and these cavities' shapes help with the insertion of these devices[6,7, 8]

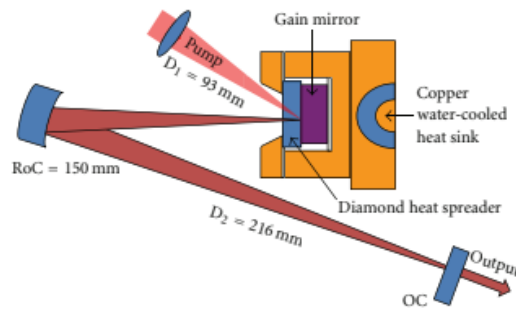


Figure 30: Diagram of V-Cavity VECSEL[8]

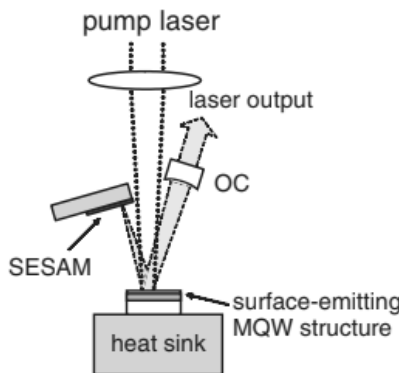


Figure 31: Diagram of V-Cavity VECSEL[6]

Figure 31 and 32 both show the most common VECSEL cavity type, the V cavity [6,7]. Figure 32 shows the most basic version, where this cavity allows for a more compact laser and better beam manipulation due to the insertion of a mirror with a radius [8]. Figure 32 shows another V cavity with a slightly different setup [6]. The most important feature to note and one of the benefits of this cavity is that it allows for the SESAM to be inserted into the cavity[6]. SESAMs are the key to controlling the loss in the system. This application of SESAMs makes this cavity-type very beneficial in controlling the beam properties of these lasers [6].

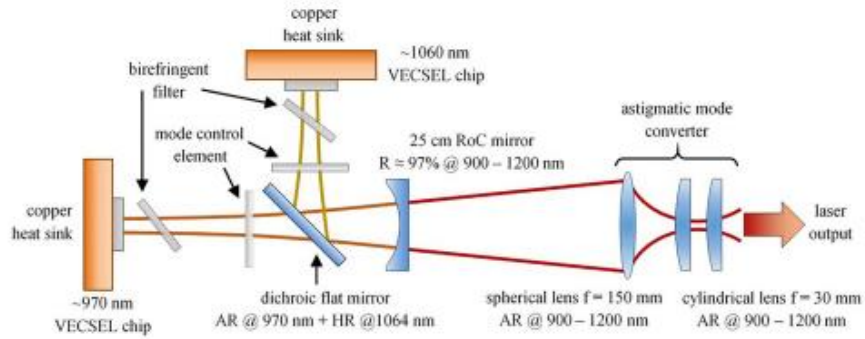


Figure 32: Diagram of T-Cavity VECSEL with additional optical devices incorporated [7]

Figure 33 shows a T cavity VECSEL [7]. T cavity VECSELs are one of the more complicated types of cavities, but it allows many interesting aspects to be accomplished. One of the main reasons for T cavities is to make two colors in one laser, which has many scientific applications [7]. More importantly for the application of this paper are the mode control elements, astigmatic mode converters, and filters [7]. These optical devices will be critical in creating a high-power 1310nm OAM laser. This external cavity shows how they can be incorporated into an external cavity and why choosing the correct cavity type is essential [7].

### 3.2 ABCD Matrix

#### 3.2.1 Intro

The duality of light states that in some cases, light can be treated as a wave, and in others, it needs to be treated as a ray. The model that tends to be taught first and is more intuitive and, therefore, in some ways more straightforward is to assume that it is a ray. This is called geometric optics. Geometric optics has many ways of modeling and calculating beam propagation [24]. The ray matrix method will be focused on since it is the building block for the ABCD matrix [24]. Starting with the most simple model in geometrical optics, the following assumptions are made, which is called a paraxial ray described in equation 15 [24].

$$r'(z) = \tan \theta = \sin \theta \approx \theta \quad (7)$$

Theta is defined below and expresses the slope from the parallel line from the axis, as depicted in Figure 34 [24].

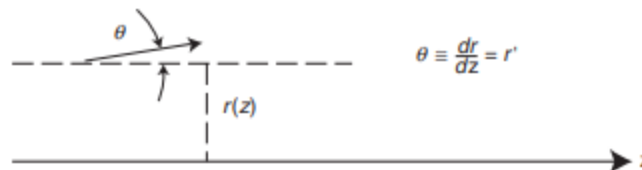


Figure 33: Model of ray matrix formula [24]

Now that the assumptions are known, two points can be found with a ray propagating through it in a vacuum [24]. The formulas in equation 16 and 17 show how this is mathematically defined.

$$r(z_2) = r(z_1) + r'(z_1)(z_2 - z_1) \quad (8)$$

$$r'(z_2) = r'(z_1) \quad (9)$$

From there, this is put into matrix notation, per equation 18.[24].

$$\begin{bmatrix} r(z_2) \\ r'(z_2) \end{bmatrix} = \begin{bmatrix} 1 & z_2 - z_1 \\ 0 & 1 \end{bmatrix} \begin{bmatrix} r(z_1) \\ r'(z_1) \end{bmatrix} \quad (10)$$

This is the matrix form of light propagating through a vacuum, which helps derive a ray's matrix form, defined in equation 19. [24].

$$\begin{bmatrix} r \\ r' \end{bmatrix} \quad (11)$$

This matrix is made up of the location of the ray propagation and the slope[24]. The free-space propagation is defined below by converting this into the more standard variables, defined below in equation 20.

$$\begin{bmatrix} r_f \\ r'_f \end{bmatrix} = \begin{bmatrix} 1 & d \\ 0 & 1 \end{bmatrix} \begin{bmatrix} r_i \\ r'_i \end{bmatrix} \quad (12)$$

This example is the simplest form of how the matrices in this method are derived, but a similar methodology and mathematical process is used for all of the other optical elements and their matrices [24]. When put into its most standard form, the ABCD matrix method is displayed in equation 21[24].

$$\begin{bmatrix} r_f \\ r'_f \end{bmatrix} = \begin{bmatrix} A & B \\ C & D \end{bmatrix} \begin{bmatrix} r_i \\ r'_i \end{bmatrix} \quad (13)$$

Modeling light in matrices simplifies the ability to do more complex systems. Moreover, it significantly decreases the difficulty of simulating and modeling beams in computers, specifically in MATLAB and similar software. However, when it comes to lasers, transverse modes and other vital features are heavily dependent on the wavelike property of light; thus, the ABCD law is used to include these properties[24]. The beam properties are related to the geometrical optical methods through the Gaussian beam intensity profile and the solution shown in equations 22 and 23.[24].

$$I(x, y, z) \sim |\epsilon_0|^2 e^{-\frac{2(x^2+y^2)}{w^2}} \quad (14)$$

$$\varepsilon_0(r) = A e^{\left(\frac{ik(x^2+y^2)}{2q(z)}\right)} e^{ip(z)} \quad (15)$$

The values "q" and "p" define the change of the gaussian beam versus the z-axis, and these parameters connect the geometrical matrices to the Gaussian beam properties[24]. Through analysis of the wavelike propagation of the light through space and other optical elements, the ABCD law was found, which describes that the transformation of a gaussian beam can be directly correlated to the geometrical optical transformation[24]. This relation is shown below in equation 24[24].

$$q_f = \frac{Aq_i + B}{Cq_i + D} \quad (16)$$

This connection allows for the relationship of the geometrical optics to the following equations 25-31 that are key to proper Gaussian beam analysis[24].

$$E(r) = \varepsilon(r) e^{-i\omega t} \quad (\text{electric field}) \quad (17)$$

$$\varepsilon(r) = \frac{Aw_0}{w(z)} e^{i(kz - \tan^{-1}(\frac{z}{z_0}))} e^{\frac{ik(x^2+y^2)}{2R(z)}} e^{-\frac{(x^2+y^2)}{w^2(z)}} \quad (18)$$

$$I(r) = \frac{c\varepsilon_0}{2} |A|^2 e^{-\frac{2(x^2+y^2)}{w^2(z)}} \quad (\text{intensity}) \quad (19)$$

$$w(z) = w_0 \sqrt{1 + \frac{z^2}{z_0^2}} \quad (\text{spot size}) \quad (20)$$

$$R(z) = z + \frac{z_0^2}{z} \quad (\text{radius of curvature}) \quad (21)$$

$$z_0 = \frac{\pi w_0^2}{\lambda} \quad (\text{Rayleigh range}) \quad (22)$$

$$\theta = \frac{\lambda}{\pi w_0} \quad (\text{divergence angle}) \quad (23)$$

The most critical of these parameters is the divergence angle, the Rayleigh range, the radius of curvature, beam waist, and the spot size[24]. Figure 35 shows a visual representation of these parameters.

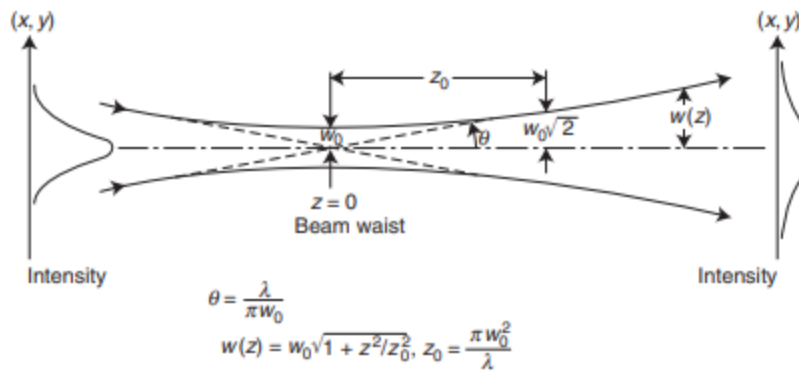


Figure 34: Model of the beam diagram and critical beam parameters[24]

The spot size is the radii of the beam relative to the z axis[24]. The beam waist is the smallest spot size of the beam and is labeled  $w_0$ [24]. Divergence angle is the angle the beam expands as it moves away from the beam waist[24]. Rayleigh Range is the length of the smallest spot size starting at the beam waist, and it measures from the beam waist to the square root of 2 times the beam waist [24]. The radius of curvature measures the radii of the wavefront[24].

Using these matrices allows for the model and simulation of a laser's beam cavity to be quickly made, which is the method used to prepare a simulation for the design of this 1310nm VECSEL. A software program was designed that allows for critical analysis of the cavity's radii, length, and other features and to determine possible design parameters for the 1310 nm VECSEL; the following explanation of the code and use of ABCD matrices will help to show the criticality of the results.

### 3.2.2 ABCD Sample Matrices

As explained, ABCD is a critical tool for inputting beams into the matrix software and evaluating beam profiles. An analysis of the standard matrices used to represent optical components will be shown and explained so that the usefulness and applications of the inputs relative to the design can be better understood later.

Free space propagation		$\begin{bmatrix} 1 & \frac{L}{n} \\ 0 & 1 \end{bmatrix}$
Thin lens		$\begin{bmatrix} 1 & 0 \\ -\frac{1}{f} & 1 \end{bmatrix}$
Spherical mirror		$\begin{bmatrix} 1 & 0 \\ -\frac{2}{R} & 1 \end{bmatrix}$
Spherical dielectric interface		$\begin{bmatrix} 1 & 0 \\ \frac{n_2 - n_1}{n_2} & \frac{1}{R} \frac{n_1}{n_2} \end{bmatrix}$

Figure 35: Ray Matrices for some common cases [13]

When it comes to lasers, the most crucial ray matrices are free-space propagation and spherical mirrors due to how the cavities are usually formed. In the free space propagation matrix,  $L$  describes the distance, and  $n$  represents the index of refraction [13]. In the spherical mirror matrix,  $R$  is the radii of the mirror. An important note is that a spherical mirror can be made into a flat mirror by assuming that the radius is infinite.

Using ABCD matrices makes this simulation easy as it becomes a combination of free space and spherical mirrors. However, there is one matrix that is not defined in Figure 36, which is essential for the analysis of V cavity VECSEL, which is for the fold mirror, which has different focal points in the tangential( vertical) and sagittal (horizontal) directions[31]. This folding mirror is more precisely just a spherical mirror that has the light coming at an angle to it and but only in one direction, thus changing the focus in only one direction, and this mirror is the connection point of the "V". In Figure 31, this is the mirror with the ROC=150mm. The matrix for these mirrors is defined in equation 32 and 33.[31]

$$\text{Reflection from spherical mirror( sagittal): } M = \begin{bmatrix} 1 & 0 \\ -\frac{2}{R \cos(\theta)} & 1 \end{bmatrix} \quad (24)$$

$$\text{Reflection from spherical mirror( tangential) : } M = \begin{bmatrix} 1 & 0 \\ -\frac{2 \cos(\theta)}{R} & 1 \end{bmatrix} \quad (25)$$

The theta is defined as half the fold angle, where the fold angle is the difference in angle between the entry and exiting beam[31]. Due to the different focuses produced by this mirror, there will be different beam profiles in the vertical and horizontal directions [31]. Two ABCD matrices will be necessary to simulate the beam appropriately[31].

With this in mind, the investigation into the inputs, outputs, and uses of the simulation can be explored.

### 3.3 ABCD Beam Profile V- Cavity VECSEL Simulation

The main intention of this paper was to do some initial investigations into how a VECSEL should be designed to accomplish the power and wavelength that will be further investigated in the future and has potential market benefits. The previous section helped design the VECSEL chip that would be used and gave possible solutions. This simulation helps with the cavity design of the laser by determining the beam profile and the area ratio. These inputs are crucial to determining the cavity parameters that need to be determined.

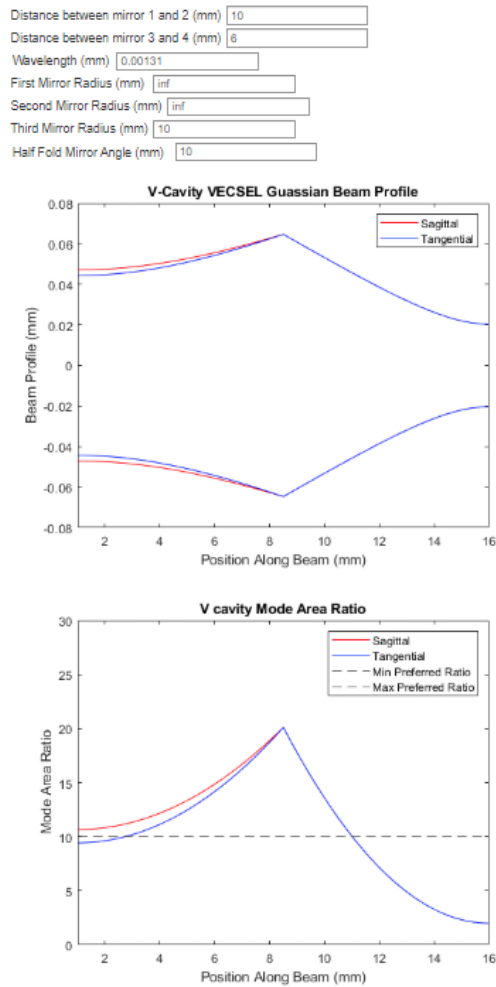


Figure 36: Graphic User Interface of the ABCD Matrix Live Program

In Figure 37 is the GUI of the tool that was made to help determine the cavity parameters. Originally the code was made in the standard MATLAB code format, but after assessing the application of this program, it was converted into a Live MATLAB code. The live MATLAB code allows for live changes that increase the code's ability to experiment, make quick changes, and troubleshoot. The code starts with defining the parameters defined in the GUI: distance between mirror 1 and 2, distance between mirror 2 and 3, wavelength, first mirror radii, second mirror radii, third mirror radii, and half fold mirror angle.

These parameters are all that is necessary to model a V cavity VECSEL beam profile in Matlab properly. Each of these inputs relates to one of the optical element matrices defined previously. These optical element matrices are multiplied in the following fashion to model the system properly.

$$\begin{bmatrix} 1 & d_{12} \\ 0 & 1 \end{bmatrix} \begin{bmatrix} 1 & -2 * \frac{\cos(\phi)}{R_2} \\ 0 & 1 \end{bmatrix} \begin{bmatrix} 1 & d_{23} \\ 0 & 1 \end{bmatrix} \begin{bmatrix} 1 & -\frac{2}{R_3} \\ 0 & 1 \end{bmatrix} \begin{bmatrix} 1 & d_{23} \\ 0 & 1 \end{bmatrix} \begin{bmatrix} 1 & -2 * \frac{\cos(\phi)}{R_2} \\ 0 & 1 \end{bmatrix} \begin{bmatrix} 1 & d_{12} \\ 0 & 1 \end{bmatrix} \begin{bmatrix} 1 & -\frac{2}{R_1} \\ 0 & 1 \end{bmatrix} \quad (26)$$

$$\begin{bmatrix} 1 & d_{12} \\ 0 & 1 \end{bmatrix} \begin{bmatrix} 1 & -\frac{2}{\cos(\phi) * R_2} \\ 0 & 1 \end{bmatrix} \begin{bmatrix} 1 & d_{23} \\ 0 & 1 \end{bmatrix} \begin{bmatrix} 1 & -\frac{2}{R_3} \\ 0 & 1 \end{bmatrix} \begin{bmatrix} 1 & d_{23} \\ 0 & 1 \end{bmatrix} \begin{bmatrix} 1 & -\frac{2}{\cos(\phi) * R_2} \\ 0 & 1 \end{bmatrix} \begin{bmatrix} 1 & d_{12} \\ 0 & 1 \end{bmatrix} \begin{bmatrix} 1 & -\frac{2}{R_1} \\ 0 & 1 \end{bmatrix} \quad (27)$$

$d_{12}$  = distance between mirror 1 and 2

$d_{23}$  = distance between mirror 2 and 3

$R_1$  = 1st mirror radii

$R_2$  = 2nd mirror radii

$R_3$  = 3rd mirror radii

$\phi$  = fold angle

Two different matrices are being multiplied due to the tangential and sagittal beam profiles made from the angular fold mirror. The above matrices only take care of one point of the z location. This location needs to be moved to model the rest of the beam; therefore, a for loop is used where the z location is moved. This is done through the use of the following matrices being used to move the location.

$$\begin{bmatrix} 1 & d - z \\ 0 & 1 \end{bmatrix} \quad (28)$$

$$\begin{bmatrix} 1 & z \\ 0 & 1 \end{bmatrix} \quad (29)$$

$$\begin{bmatrix} 1 & d + d1 - z \\ 0 & 1 \end{bmatrix} \quad (30)$$

$$\begin{bmatrix} 1 & x - z \\ 0 & 1 \end{bmatrix} \quad (31)$$

Using all of these different matrices and multiplying them in MATLAB create the GUI, and the outputs are shown. The first graph shows the beam profile of the VECSEL being modeled. The first important factor that might be noticed is the difference in the sagittal and tangential beams, which is also shown by the need for two different cavity matrices. This difference will help ensure that the fold angle does not become too large and that issues start to form with the non-spherical shape of the beam. Another feature is that it can tell if the beam is stable or not. A stable laser is defined as a beam remaining within the resonator indefinitely[24].

In contrast, an unstable laser will eventually escape the resonator after a certain number of reflections[24]. Some lasers operate well in an unstable state, but the VECSEL being designed will not be. The shape or radii at specific locations is also vital due to highlighting areas where other optical components can be placed into the beam with the appropriate beam size.

The second graph shows the mode area ratio. Its necessity in laser design will be explained to define the mode area ratio. To mode lock a VECSEL, the absorber( SESAM) has to saturate before the gain in order to mode lock the lazer[31]. Mode locking is a technique that produces high power short pulse laser and it is commonly used in VECSELS[31]. This result will be a net gain window forming where the loss of the absorber is reduced below the gain [31]. The function for the ratio that will determine the region where this will happen is shown below[31].

$$S_{area} = \frac{E_{sat,g}}{E_{sat,a}} = \frac{F_{sat,g}A_g}{F_{sat,a}A_a} = \frac{A_g}{A_a} \gg 10 \quad (32)$$

The reduction seen above is due to the similarities between the QW materials and the SESAM [31]. This reduction leads to the mode area ratio being the ratio of the gain chip's physical mode area versus the SESAM's physical mode area [31]. On the graph, the y value between 10x and 30x corresponds to the x location where the SESAM can be placed the lasing will be able to occur[31].

This simulation is a tool that can be used throughout the initial design phase, the preparation phase, the implementation phase, and the optimization phase. The initial design can determine the location of all the necessary parts of the cavity, the radii, and the fold angle. During the initial design, decisions on which mirrors to buy, how much room will be available, and other similar aspects of the design will be decided. This decision of the initial design can be dialed in using this tool and assisting in transitioning from the theoretical space where everything is precisely how it is needed and the practical space where there are finite options available with possible

cost and quality differences between the options. During the preparation and implementation phases, this simulation's real-time input and output allow for quick checking of many different variables and situations, which is helpful when troubleshooting or changes are necessary. The real-time input and output capabilities allow for quick and numerous checks while adjusting the system. All in all, this is a tool that creates a live assessment of the system and the beam profile that is being made. This is critical in complex systems such as lasers because of the many variables that can be uncertain and the unexpected changes that can happen in any project.

## Chapter 4: Compensating Spatial Walkoff using Phase Shifted Astigmatic Mode Converter

### 4.1 Introduction/ Background

The last section will focus on something not for general VECSELs but is trying to find a solution to a more specific issue seen on similar VECSEL designs like this one. The issue is that the spatial walk-off of the laser introduces distortion. The solution for this distortion being investigated is to use a tilted astigmatic mode converter, hoping that a partially converted beam will compensate for the distortion.

Earlier in this paper, the importance of the higher transverse modes was discussed for the OAM applications that this laser is being designed for; the creation of these higher modes usually includes the use of a birefringent crystal, which means that it has a different index of refraction in the optical axis. During the use of these crystals, a walk-off can be created. Spatial walk-off is defined as an angular deviation of the extraordinary beam, Figure 38 shows a visual representation of this[32]. In the sense of this situation, the extraordinary beam or "e" beam shown in Figure 38 refers to the orthogonally polarized light which is interacting with the birefringent crystal, which is tilted at an angle " $\zeta$ " [32,39].

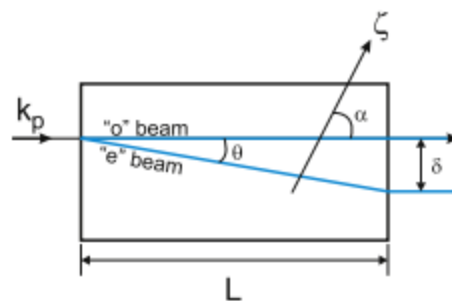


Figure 37: Diagram of spatial walk-off effect [32]

One of the effects of this walk-off is that it produces distortion in the higher modes, of which a practical example is in Figure 39[32,33].

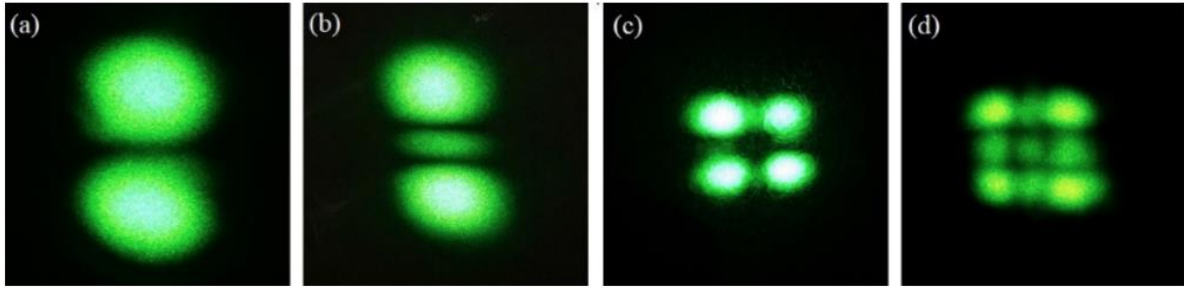


Figure 38: Experimental images of SHG beams including  $HG_{01}, HG_{02}, HG_{11}$  and  $HG_{22}$  [33]

Astigmatic Mode converters can convert a Laguerre-gaussian Beam to a Hermite Gaussian Beam and vice versa[34]. The basic theory revolves around the equation below[34].

$$u_{nm}^{LG}(x, y, z) = \sum_{k=0}^N i^k b(n, m, k) u_{N=k,k}^{HG}(x, y, z) \quad (33)$$

With real coefficients

$$b(n, m, k) = \left( \frac{(N-K)! k!}{2^N n! m!} \right)^{\frac{1}{2}} * \frac{1}{k!} \left( \frac{d^k}{dt^k} \right) [(1-t)^n (1+t)^m]_{t=0} \quad (34)$$

Figure 40 models this formula and highlights what it means visually[34].

(nm)	
02	$\bigcirc = \frac{1}{2} \begin{matrix} \bullet \\ \bullet \end{matrix} + \frac{i}{\sqrt{2}} \begin{matrix} \bullet \\ \bullet \end{matrix} - \frac{1}{2} \begin{matrix} \bullet \\ \bullet \end{matrix}$
11	$\odot = \frac{1}{\sqrt{2}} \begin{matrix} \bullet \\ \bullet \end{matrix} + \frac{1}{\sqrt{2}} \begin{matrix} \bullet \\ \bullet \end{matrix}$
20	$\bigcirc = \frac{1}{2} \begin{matrix} \bullet \\ \bullet \end{matrix} - \frac{i}{\sqrt{2}} \begin{matrix} \bullet \\ \bullet \end{matrix} - \frac{1}{2} \begin{matrix} \bullet \\ \bullet \end{matrix}$
02	$\begin{matrix} \bullet \\ \bullet \end{matrix} = \frac{1}{2} \begin{matrix} \bullet \\ \bullet \end{matrix} + \frac{1}{\sqrt{2}} \begin{matrix} \bullet \\ \bullet \end{matrix} + \frac{1}{2} \begin{matrix} \bullet \\ \bullet \end{matrix}$
11	$\oplus = \frac{1}{\sqrt{2}} \begin{matrix} \bullet \\ \bullet \end{matrix} - \frac{1}{\sqrt{2}} \begin{matrix} \bullet \\ \bullet \end{matrix}$
20	$\begin{matrix} \bullet \\ \bullet \end{matrix} = \frac{1}{2} \begin{matrix} \bullet \\ \bullet \end{matrix} - \frac{1}{\sqrt{2}} \begin{matrix} \bullet \\ \bullet \end{matrix} + \frac{1}{2} \begin{matrix} \bullet \\ \bullet \end{matrix}$

Figure 39: Examples of the decomposition of HG and LG modes [34].

In equation 41,  $u_{nm}^{HG}$  represents HG transverse mode beam equation, and  $u_{nm}^{LG}$  represents the LG transverse mode beam equation[34]. The equation above shows that the LG beam can be decomposed into a set of HG mode beams of the same order dependent on "b", which are the real coefficients, and " $i^k$ ," which corresponds to the  $\pi/2$  relative phase difference between successive

components[34]. Another important note is that an HG model can be decomposed into the same b coefficients if the z-axis is at a 45° angle with the x and y axis as shown in equation 43.

$$u_{nm}^{HG} \left( \frac{x+y}{\sqrt{2}}, \frac{x-y}{\sqrt{2}}, z \right) = \sum_{k=0}^N b(n, m, k) u_{N=k,k}^{HG}(x, y, z) \quad (35)$$

The above equations can be proven through operator algebra and direct comparison with a 2D quantum harmonic oscillator[34].

These equations make it apparent that it is necessary to rephrase the terms in the decomposition[34]. The correct path to rephasing is through the Gouy phase[34]. The Gouy phase is defined as the phase shift of the beam going through the beam waist compared to the phase shift if a plane wave went through the beam waist[34].

Equations 44-48 shows the portion of the equation that relates to the Gouy Shift and how it is defined for a regular and an astigmatic beam[34].

$$(n + m + 1)\Psi(z) \quad (36)$$

$$\Psi(z) = \arctan \left( \frac{z}{z_r} \right) \quad (37)$$

$$\left( n + \frac{1}{2} \right) \Psi_x(z) + \left( m + \frac{1}{2} \right) \Psi_y(z) \quad (38)$$

$$\Psi_x = \arctan \left[ \frac{z - z_{0x}}{z_{Rx}} \right] \quad (39)$$

$$\Psi_y = \arctan \left[ \frac{z - z_{0y}}{z_{Ry}} \right] \quad (40)$$

The end goal is to have the Gouy Phase shift equal to  $i^k$ , seen in the original decomposition, thus allowing for the HG to be converted to LG[34]. The astigmatic properties of the Gouy phase will be used to create a Gouy Phase shift that will equal the required  $i^k$ , allowing the original decomposition formula to complete the HG to LG switch[34]. This switch is done by creating an astigmatic region where the shift can be completed, which can be done by using two cylindrical lenses placed at the beam waist transverse radii and with corresponding focal lengths[34]. A model of this is shown in Figure 41[34].

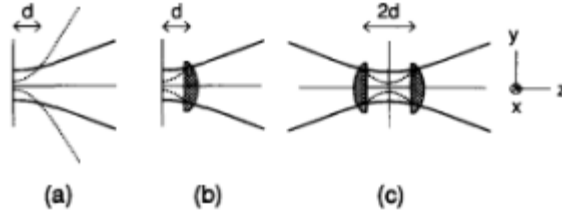


Figure 40: Beam profile (a), a lens placed at the beam waist transverse radii (b), and two lenses placed at each of the beam waists transverse radii (c)

Using this apparatus, the change in the Gouy phase can be calculated, and then the  $i^k$  value shown below can be derived[34].

$$\theta = 2\left[\arctan\left(\frac{d}{z_{Rx}}\right) - \arctan\left(\frac{d}{z_{Ry}}\right)\right] = 2\left[\arctan\left(\frac{1}{p}\right) - \arctan(p)\right] \quad (41)$$

When this value is set to  $\pi/2$ , then it completes the requirement for the HG to LG switch[34]. This derivation is how an astigmatic mode converter can change a beam from HG to LG[34].

The goal of simulating an AMC on a beam with a walk-off is to find a new way to compensate for the introduced walk-off. The hypothesis is that there might be an angle at which the distortion caused by the AMC apparatus being at a Gouy angle different from the ideal  $\pi/2$  would reverse or dampen the distortion caused by spatial walk-off [34].

This compensation would be accomplished by experimentally going through values from 0 to  $\pi/2$  of the Gouy Phase shift previously described as  $\pi/2$  for the perfect theoretical conversion. The math required to find this theoretically would be intensive or impossible. Primarily due to assumptions needed to make the math easier not being applicable once the ideal is left; therefore, simulating the experiment is the best way to check if this is a viable option.

## 4.2 Astigmatic Mode Converter Theory and Code Simulation

As mentioned above, the code needs to accomplish the theoretical effect of an astigmatic mode converter on a beam with walk-off. After that, the Gouy phase shift will be changed in hopes that the converter used at a non-ideal Gouy angle will reverse the distortion caused by the spatial walk-off.

To start this simulation, the x,y, and z parameters are defined in matrix form so that Matlab can correctly compute them. The number of steps used to create this coordinate system is crucial because it determines the simulation's accuracy and the length of time required to complete it.

With the coordinate system created, the next step is to define the beam and the AMC. This step includes the LG mode order, wavelength, crystal length, walk-off parameter, refractive index, and nonlinearity. With these parameters defined, the beam can be simulated[34].

With these defined, the effect of the AMC can be initiated on the beam. The code for the LG to HG starts with defining the superposition coefficients shown in equation 42[34].

Following that, the HG function is defined below[34].

$$u_{nm}^{HG}(x, y, z) = C_{nm}^{HG} \left( \frac{1}{w} \right) e^{-\frac{ik(x^2+y^2)}{2R}} * e^{-\frac{x^2+y^2}{w^2}} * e^{-i(n+m+1)\Psi} \quad (42)$$

$$* H_n \left( \frac{x\sqrt{2}}{w} \right) H_m \left( \frac{y\sqrt{2}}{w} \right)$$

All of the variables in the equation are already defined in the initial parameters or are defined in the following two figures[34].  $R$  is the Rayleigh range, and  $\Psi$  is the Gouy Phase[34].

$$R(z) = \frac{(z_R^2 + z^2)}{2z} \quad (43)$$

$$\frac{1}{2} kW^2(z) = \frac{(z_R^2 + z^2)}{z_R} \quad (44)$$

$$\Psi(z) = \arctan \left( \frac{z}{z_R} \right) \quad (45)$$

$$C_{nm}^{HG} = \left( \frac{2}{\pi n!} \right)^{\frac{1}{2}} 2^{-\frac{N}{2}} \quad (46)$$

$$C_{nm}^{LG} = \left( \frac{2}{\pi n! m!} \right)^{\frac{1}{2}} \min(n, m) \quad (47)$$

All of the necessary parameters have been defined for the HG beam to be simulated; the  $i^k$  value can be applied to see what changing the Gouy Phase Shift effect is[34].

With the HG beam defined, the next step propagates the actual beam so that it can be analyzed through the entire distance desired. Using the transfer function is one of the best ways to simulate optics in Matlab, and this is what was used to simulate the propagation of the beam. In short, it requires that the defined beam is moved into the frequency coordinates using Fourier Shift and the frequency coordinates mentioned before. Then multiply the new beam in frequency space by the transfer function. Finally, this is inversely Fourier transferred to bring it back into the spatial coordinate system. This process is done in a for loop through every defined  $z$  point. This process allows the beam to be defined at every  $z$  value with the full  $x$  and  $y$  beam profile. This portion is also when the walk-off is applied. Thus, a transfer function is needed for the beam with and without walk-off to make a comparison possible.

The effect has been simulated, and the beam data is stored in matrix form. The last step is plotting the data and comparing it to the data with no walk-off distortion. These results will be analyzed in the last section.

### 4.3 Results and Analysis

As mentioned previously, a simulation of an HG beam was made to test this method, and then an AMC conversion was introduced. This conversion was tested before applying any walk-off to check that it was working correctly. To test this, we changed the AMC phase to  $\pi/2$ . The value for p and l indices was also 2 and 0, respectively. The walk-off parameter is also set to 0. Following that, the ability to create HG was checked, and all the parameters were kept the same, except the angle was changed to 0. Figure 42 shows the HG and LG next to each other, respectively.

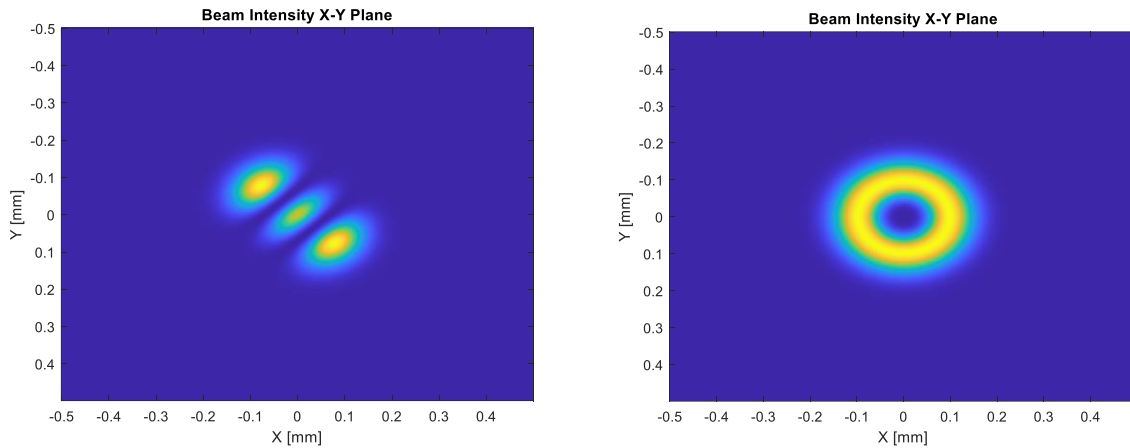


Figure 41: Beam Intensity Profile of HG and LG fundamental beams at  $45^\circ$  with 0 walk-off parameter and  $0^\circ$  Gouy Angle Shift on the AMC simulation

Figure 42 proves that the tool can simulate the LG and HG fundamental beam at a  $45^\circ$  angle which is required for some theories to follow the correct assumptions. One important note is that to better apply this simulation to future applications, the second harmonic generation of the beam was applied, which doubles the nodes seen[40]. The double nodes are shown in Figure 43. SHG will be used to see the effect of the AMC angle on spatial walk-off distortion moving forward.

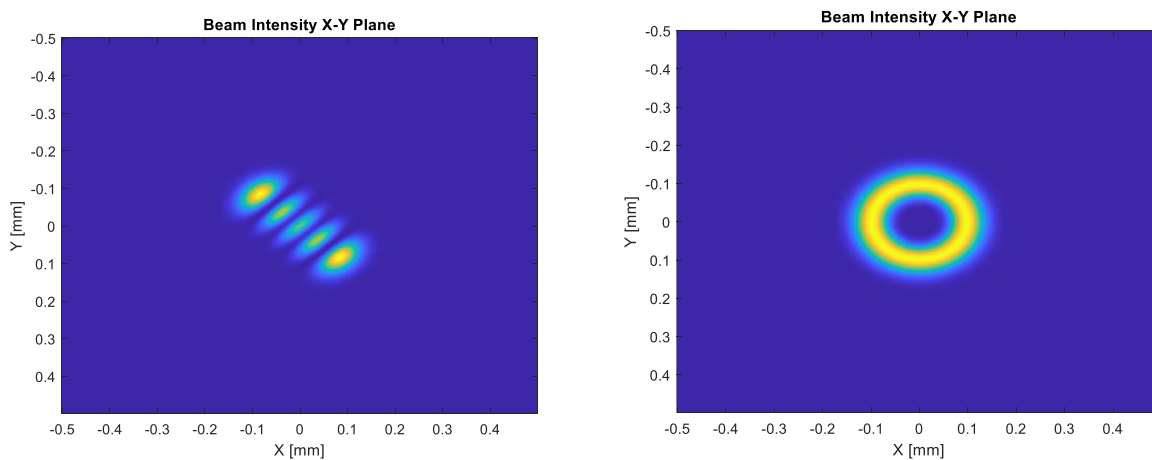


Figure 42: Beam Intensity Profile of HG and LG second harmonic generation beams at  $45^\circ$  with 0 walk-off parameter and  $0^\circ$  Gouy Angle Shift on the AMC simulation

The next step was to add the distortion. The walk-off parameter was changed to .001, and then the LG and HG mode was simulated again to show the effect of the walk-off distortion.

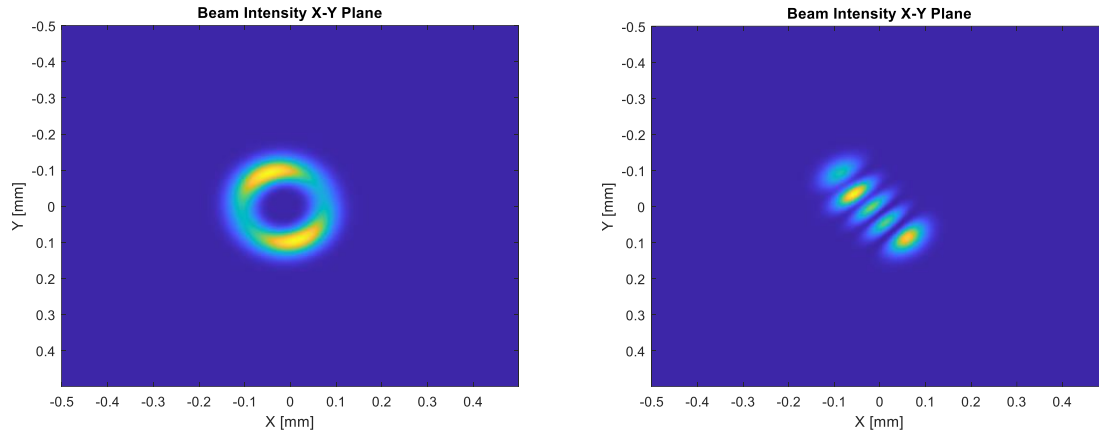


Figure 43: Beam Intensity Profile of HG and LG fundamental beams at  $45^\circ$  with .001 mm walk-off parameter and  $0^\circ$  Gouy Angle shift on the AMC simulation

The distortion tends to pool the beam's intensity in the top left and bottom right of the LG model. The intensity gradient seems to be not perfectly symmetrical but in similar shape and size in the two areas of higher intensity. For the HG mode, the higher intensity moves away from the top node and goes to the second to last node. There is also a slight curvature that can now be seen on the node line. Begin experimentally compensating for this distortion,  $.5 * \pi/2$  was chosen to see what the effect would be, displayed in Figure 45.

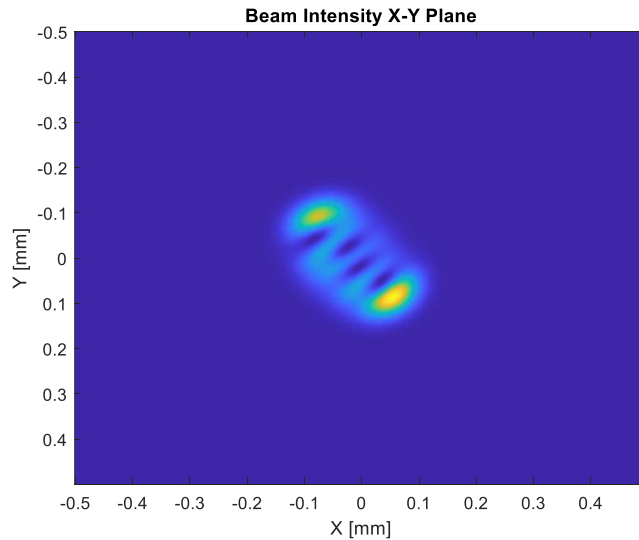


Figure 44: Beam Intensity Profile of Beam at  $45^\circ$  with 0.001 mm walk-off parameter and  $0.5 * \pi/2$  Gouy Angle Shift on the AMC simulation

With the 0.5 angle, the beam is twisted and does not represent an improvement for an LG or HG beam. There are still strange locations and a visible twist for the higher intensity location.

Therefore 0.25 and 0.75 were chosen for the following angles choices to see if getting closer to LG or HG was better at compensating for the distortion displayed in Figure 46.

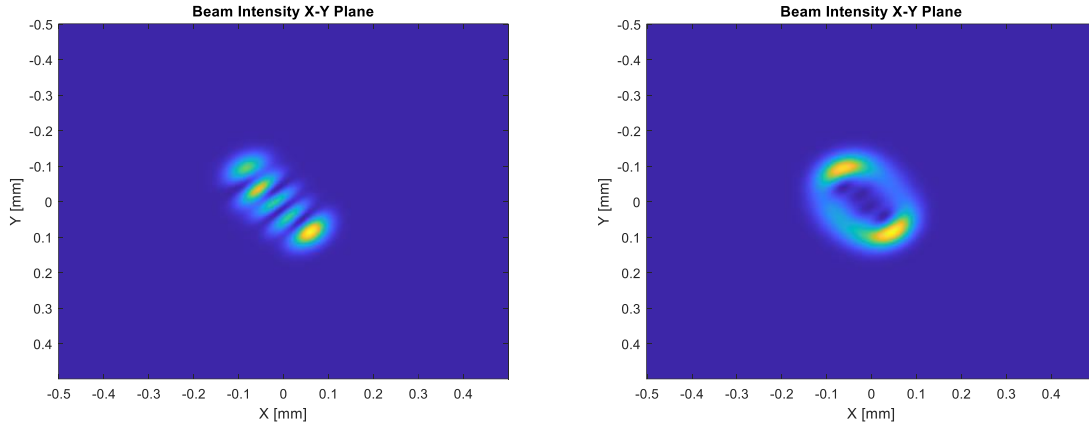


Figure 45: Beam Intensity Profile of Beam at  $45^\circ$  with 0.001 mm walk-off parameter and  $0.25 \cdot \pi/2$  Gouy Angle Shift (Left) and  $0.75 \cdot \pi/2$  Gouy Angle Shift (Right)

For the  $0.25 \cdot \pi/2$  there is not much improvement, the intensity is not moving in the correct direction, and the twist is not getting taken away. For 0.75, there is some reduction in the higher intensity areas in the top left and bottom right areas, but the oval shape is significant, and the shadow of the nodes from the HG is still prevalent. Due to the 0.75 multiplier compensating for the distortion the best over the 0.5 and 0.25, the following multipliers will be investigated in this order. 0.8 ,0.85, and 0.9.

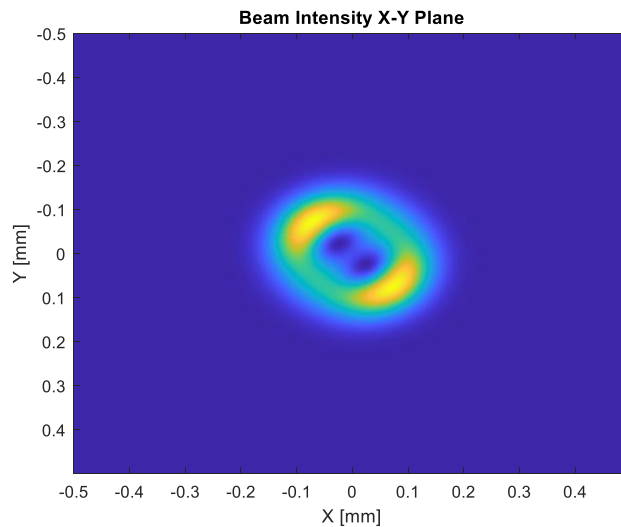


Figure 46: Beam Intensity Profile of Beam at  $45^\circ$  with 0.001 mm walk-off parameter and  $0.8 \cdot \pi/2$  Gouy Angle

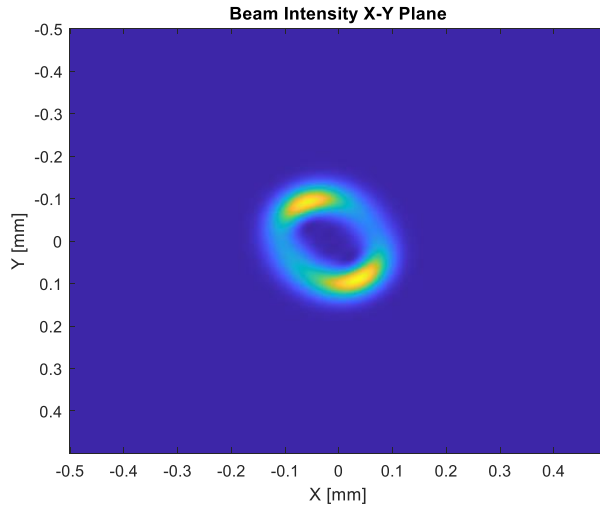


Figure 47: Beam Intensity Profile of Beam at  $45^\circ$  with 0.001 mm walk-off parameter and  $0.85 \cdot \pi/2$  Gouy Angle

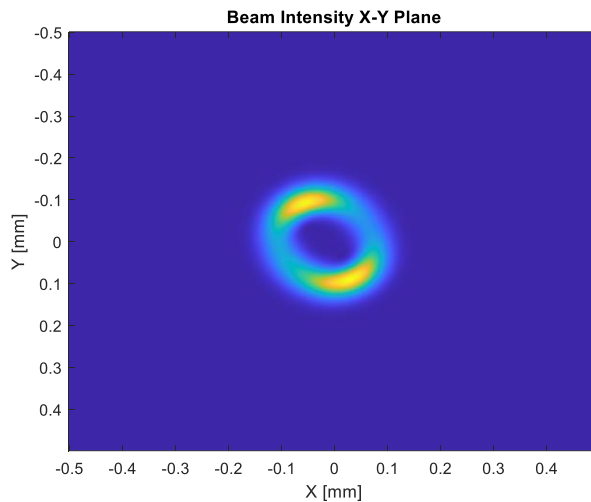


Figure 48: Beam Intensity Profile of Beam at  $45^\circ$  with 0.001 mm walk-off parameter and  $0.9 \cdot \pi/2$  Gouy Angle

From the results above displayed in Figure 49, it becomes evident that this was not an effective method for reversing the distortion. If the multiplier for the  $\pi/2$  is too tiny, it looks more like an HG, and the shape difference is significant enough that the previous distortion is probably better in most optical scenarios. It has a better structure and shape as it gets closer to the .9 multiplier. However, the distortion is already too prevalent to get rid of once it is close to  $\pi/2$ . Close to  $0.85 \cdot \pi/2$  is arguably the closest to getting rid of the distortion. However, the shape is still too oval, and the higher densities around the top of the left edge and bottom-right edges have not been entirely nullified. This value is the best because the distortion caused it to spread the higher density areas more uniform around the edges of the circles while not turning too far into another shape.

While this method is not effective, other methods can be used to reverse the distortion. Splitting or adding the birefringent crystal and making it in opposite directions to the original, thus canceling out the distortion, a practice that has seen success in other studies [39].

## Chapter 5: Conclusions

This paper has three connected but different topics: Initial Design parameters for a 1310 nm OAM VECSEL, ABCD Matrix VECSEL Beam Live Simulation, and a tilted astigmatic mode converter to compensate for spatial distortion. The outcomes will be summarized, and the next steps for future applications will be outlined for each section.

The first section investigates several essential features for designing a high-power 1310nm OAM VECSEL. The main features were the thermal management technique and material used in the quantum well structure. Other features were discussed concerning their effect on the main two parameters. Lastly, some of the complete designs of VECSEL were investigated and compared to understand what has already been successful in some dimensions of this design. The recommendation, in the end, was to use InGaAsP/InP with the flip chip method. This thermal management was chosen to avoid the risk of having the thermal management inside the beam and possibly causing issues with the higher modes that are required. The material was often used for this wavelength, and its bandgap range was closer to the correct wavelength, giving more flexibility in the redshift. This recommendation came with a couple of options in case it was unsuccessful. If thermal management was too low, then the intracavity diamond could be added later because, at that point, the thermal management risk outweighs the possibility of creating issues with higher order modes. The two studies with the highest powers used the technique that was not investigated fully due to potential issues with cost and manufacturing. If the cost and manufacturing risk could be tolerated, wafer fusion for the DBR is an option that saw success in other VECSELS. The next steps for this design are to determine the features that were not discussed in this paper. Once these are determined, then the actual design can be started. Once all the design parameters have been determined, including the cost and manufacturing capabilities of the design team, then the actual design can be started. This paper will still be helpful until the goal has been achieved because if there is any issue or it is not performing well enough, this document can be used to show other possible options.

The next section detailed the code and theory of a Live ABCD Matrix Beam profile simulation program in Matlab. The code was created using the matrix method and how it can model a V Cavity VECSEL. The program inputs are distance between mirror 1 and 2, distance between mirror 2 and 3, wavelength, first mirror radii, second mirror radii, third mirror radii, and half fold mirror angle. The output of this design is two graphs. One that shows the beam profile of the VECSEL for both the tangential and sagittal rays. The other graph shows the mode area ratio, which has an indicator line for an area mode ratio of 10. This indicator is important because for a SESAM to operate correctly, it must be above the ten indicator line. Thus this graph shows the locations adequate for the placement of the SESAM. The next steps for this code would be to

make it compatible with other types of cavities and display other information that might be helpful during the initial design and creation of a VECSEL. This design will allow the design team that will continue forward with high power 1310 nm OAM VECSEL to have instant feedback and increased ability to troubleshoot any issues or constraints that present themselves moving forward.

The last section investigated using the simulation of an astigmatic mode converter at an angle to analyze whether or not this would be able to compensate for spatial walk-off. This simulation was done using Matlab and explained the theory behind an AMC. The explanation included how the code simulated the walk-off and the AMC. The theory did not provide an immediate answer, and therefore this simulation was done to experimentally see if an angle could be found that would compensate for the distortion. The values that were checked were all  $\pi/2$  multiplied by fractions. The fractions tested were 0.5, 0.25, 0.75, 0.8, 0.85, 0.9. The best value was  $.85 * \pi/2$ , but unfortunately, it was not effective in reducing the distortion significantly. The next step would be determining a different way to compensate for this distortion. Typically this distortion is made through a birefringent crystal. Therefore, one of the other solutions is adding an identical birefringent crystal that is rotated 180 degrees to reverse the distortion. This idea could be a viable solution for solving this issue in the potential design.

# Reference

1. DeCusatis, & DeCusatis, Carolyn J. Sher. (2006). *Fiber optic essentials* (1st edition). Elsevier/Academic Press.
2. David Goff. (2002). *Fiber Optic Reference Guide*, 3rd Edition. Routledge.
3. Padgett. (2017). Orbital angular momentum 25 years on [Invited]. *Optics Express*, 25(10), 11265–11274. <https://doi.org/10.1364/OE.25.011265> Twisted Photons
4. Torres, Molina-Terriza, G., & Torner, L. (2007). Twisted photons. *Nature Physics*, 3(5), 305–310. <https://doi.org/10.1038/nphys607>
5. Bozinovic, Yue, Y., Ren, Y., Tur, M., Kristensen, P., Huang, H., Willner, A. E., & Ramachandran, S. (2013). Terabit-Scale Orbital Angular Momentum Mode Division Multiplexing in Fibers. *Science (American Association for the Advancement of Science)*, 340(6140), 1545–1548. <https://doi.org/10.1126/science.1237861>
6. Tropper, Foreman, H. D., Garnache, A., Wilcox, K. G., & Hoogland, S. H. (2004). Vertical-external-cavity semiconductor lasers. *Journal of Physics. D, Applied Physics*, 37(9), R75–R85. <https://doi.org/10.1088/0022-3727/37/9/R01>
7. Lukowski, Hessenius, C., Meyer, J. T., Wright, E. M., & Fallahi, M. (2018). High power two-color orbital angular momentum beam generation using vertical external cavity surface emitting lasers. *Applied Physics Letters*, 112(4), 41108. <https://doi.org/10.1063/1.5009090>
8. Sirbu, Volet, N., Mereuta, A., Lyytikäinen, J., Rautiainen, J., Okhotnikov, O., Walczak, J., Wasiaak, M., Czystanowski, T., Caliman, A., Zhu, Q., Iakovlev, V., & Kapon, E. (2011). Wafer-Fused Optically Pumped VECSELs Emitting in the 1310-nm and 1550-nm Wavebands. *Advances in Optical Technologies*, 2011, 1–8. <https://doi.org/10.1155/2011/209093>
9. Sirbu, Rantamäki, A., Iakovlev, V., Mereuta, A., Caliman, A., Volet, N., Lyytikäinen, J., Okhotnikov, O., & Kapon, E. (2015). Recent progress in wafer-fused VECSELs emitting in the 1310nm waveband. 9349, 934907–934907–7. <https://doi.org/10.1117/12.2079752>
10. Tropper, Foreman, H. D., Garnache, A., Wilcox, K. G., & Hoogland, S. H. (2004). Vertical-external-cavity semiconductor lasers. *Journal of Physics. D, Applied Physics*, 37(9), R75–R85. <https://doi.org/10.1088/0022-3727/37/9/R01>
11. Sirbu, Mereuta, A., Rautiainen, J., Lyytikäinen, J., Caliman, A., Okhotnikov, O., & Kapon, E. (2009). High power vertical external cavity surface-emitting lasers (VECSELs) emitting in 1310 nm and 1550 nm bands. 2009 IEEE LEOS Annual Meeting Conference Proceedings, 835–836. <https://doi.org/10.1109/LEOS.2009.5343423>
12. Murshid, & Morgan & Claypool Publishers, publisher. (2018). *Optical fiber multiplexing and emerging techniques : SDM and OAM*.
13. Svelto. (2009). *Principles of Lasers*. Springer.
14. Tan. (2005). *High operating temperature of passively mode-locked InGaAsP/InP semiconductor lasers*. ProQuest Dissertations Publishing.
15. Rantamäki, Sirbu, A., Saarinen, E. J., Lyytikäinen, J., Mereuta, A., Iakovlev, V., Kapon, E., & Okhotnikov, O. G. (2014). High-power flip-chip semiconductor disk laser in the 1.3  $\mu\text{m}$  wavelength band. *Optics Letters*, 39(16), 4855–4858. <https://doi.org/10.1364/OL.39.004855>
16. Mangold, Wittwer, V. J., Sieber, O. D., Hoffmann, M., Krestnikov, I. L., Livshits, D. A., Golling, M., Südmeyer, T., & Keller, U. (2012). VECSEL gain characterization. *Optics Express*, 20(4), 4136–4148. <https://doi.org/10.1364/OE.20.004136>

17. Tsang, & Tsang, W. T. (1985). Semiconductors and semimetals a treatise. Volume 22, Lightwave communications technology. Part C, Semiconductor injection lasers. II, Light-emitting diodes.
18. Jiann S. Yuan. (1999). SiGe, GaAs, and InP Heterojunction Bipolar Transistors. Wiley-Interscience.
19. Zhang. (2011). Gas Source MBE Grown Wavelength Extending InGaAs Photodetectors. IntechOpen. <https://doi.org/10.5772/13910>
20. Masood, Amarasinghe, N. V., McWilliams, S., Patterson, S., Roh, D., Evans, G. A., & Butler, J. (2005). High-temperature continuous-wave operation of 1310-nm single-mode grating-outcoupled surface-emitting semiconductor lasers. *Proc. SPIE*, 5738(1), 271–284. <https://doi.org/10.1117/12.591827>
21. McWilliams, Amarasinghe, N. V., Masood, T., Shi, H., & Evans, G. A. (2006). Long-wavelength multiwatt 1310 and 1550-nm grating-outcoupled surface-emitting semiconductor lasers. *Proceedings of SPIE*, 6287(1), 628704–6287010. <https://doi.org/10.1117/12.683454>
22. Masood, Patterson, S., Evans, G. ., Kirk, J. ., Hilali, Z. ., Amarasinghe, N. ., Phan, D., & Lee, D. (2003). 1310 nm grating-outcoupled surface-emitting semiconductor lasers. Conference on Lasers and Electro-Optics, 2003. CLEO '03, 1157–1158.
23. Ivanov, Kurnosov, V. D., Kurnosov, K. V., Marmalyuk, A. A., Romantsevich, V. I., Ryaboshan, Y. L., & Chernov, R. V. (2007). Refractive indices of solid AlGaInAs solutions. *Quantum Electronics (Woodbury, N.Y.)*, 37(6), 545–548. <https://doi.org/10.1070/QE2007v037n06ABEH013442>
24. Milonni, Eberly, & Eberly, J. H. (2010). Laser physics. John Wiley & Sons.
25. Grundmann. (n.d.). The Physics of Semiconductors (4th ed. 2021). Springer International Publishing. <https://doi.org/10.1007/978-3-030-51569-0>
26. Saadallah, Yacoubi, N., Genty, F., & Alibert, C. (2002). Investigation of thermal and optical properties of distributed Bragg reflectors by photothermal deflection spectroscopy. *Applied Optics*, 41(36), 7561–7568. <https://doi.org/10.1364/AO.41.007561>
27. Okhotnikov. (2010). Semiconductor Disk Lasers. John Wiley & Sons, Incorporated.
28. Jin, Sweeney, S. J., Adams, A. R., Higashi, T., Riechert, H., & Thijs, P. J. A. (2003). Wavelength dependence of the modal refractive index in 1.3  $\mu\text{m}$  InGaAsP, AlGaInAs and GaInNAs lasers using high pressure. *Physica Status Solidi. B. Basic Research*, 235(2), 491–495. <https://doi.org/10.1002/pssb.200301608>
29. Shimizu, Babić, D. I., Dudley, J. J., Jiang, W. B., & Bowers, J. E. (1993). Thermal resistance of 1.3 $\mu\text{m}$  InGaAsP vertical cavity lasers. *Microwave and Optical Technology Letters*, 6(8), 455–457. <https://doi.org/10.1002/mop.4650060802>
30. Kubota, Hamano, K., Takemasa, K., Kobayashi, M., Wada, H., & Munakata, T. (2000). THERMAL PROPERTIES OF 1.3  $\mu\text{m}$  AlGaInAs MULTI QUANTUM WELL RIDGE WAVEGUIDE LASERS. *Jpn.J.Appl.Phys ,Part 1. Vol. 39, No. 4B, Pp. 2297-2300. 2000, 39(4B), 2297–2300.*
31. Meyer, Fallahi, M., Wright, E. M., Pau, S. K. H., & Hessenius, C. A. (2021). Novel Cavities in Ultrafast Vertical External Cavity Surface Emitting Lasers for High Power Harmonic Generation. The University of Arizona.
32. Pérez, Just, F., Cavanna, A., Chekhova, M. V., & Leuchs, G. (2013). Compensation of anisotropy effects in a nonlinear crystal for squeezed vacuum generation. *Laser Physics Letters*, 10(12), 125201. <https://doi.org/10.1088/1612-2011/10/12/125201>

33. Lukowski, Meyer, J. T., Hessenius, C., Wright, E. M., & Fallahi, M. (2017). Generation of high-power spatially structured beams using vertical external cavity surface emitting lasers. *Optics Express*, 25(21), 25504–25514. <https://doi.org/10.1364/OE.25.025504>
34. Beijersbergen, Allen, L., van der Veen, H. E. L. ., & Woerdman, J. . (1993). Astigmatic laser mode converters and transfer of orbital angular momentum. *Optics Communications*, 96(1), 123–132. [https://doi.org/10.1016/0030-4018\(93\)90535-D](https://doi.org/10.1016/0030-4018(93)90535-D)
35. Rutz, Liverini, V., Maas, D., Rudin, B., Bellancourt, A.-R., Schon, S., & Keller, U. (2006). Passively modelocked GaInNAs VECSEL at centre wavelength around 1.3μm. *Electronics Letters*, 42(16), 926–927. <https://doi.org/10.1049/el:20061793>
36. Jetter, & Michler, P. (2021). *Vertical External Cavity Surface Emitting Lasers : VECSEL Technology and Applications*.
37. Mildren, & Rabeau, J. (2013). *Optical Engineering of Diamond* (1. Aufl.). Wiley-VCH.
38. Lukowski, Meyer, J. T., Hessenius, C., Wright, E. M., & Fallahi, M. (2019). High-Power Higher Order Hermite-Gaussian and Laguerre-Gaussian Beams From Vertical External Cavity Surface Emitting Lasers. *IEEE Journal of Selected Topics in Quantum Electronics*, 25(6), 1–6. <https://doi.org/10.1109/JSTQE.2019.2906256>
39. Dmitriev, Gurzadyan, G. G., Nikogosyan, D. N., Schawlow, A. L., & Shimoda, K. (2013). *Handbook of Nonlinear Optical Crystals* (Vol. 64). Springer Berlin / Heidelberg.
40. Dholakia, Simpson, N., Padgett, M., & Allen, L. (1996). Second-harmonic generation and the orbital angular momentum of light. *Physical Review. A, Atomic, Molecular, and Optical Physics*, 54(5), R3742–R3745. <https://doi.org/10.1103/PhysRevA.54.R3742>
41. Selmic, Tso-Min Chou, Jiehping Sih, Kirk, J. B., Mantle, A., Butler, J. K., Bour, D., & Evans, G. A. (2001). Design and characterization of 1.3-μm AlGaInAs-InP multiple-quantum-well lasers. *IEEE Journal of Selected Topics in Quantum Electronics*, 7(2), 340–349. <https://doi.org/10.1109/2944.954148>